

Graph Theoretical Analysis of local ultraluminous infrared galaxies and quasars

Orestis Pavlou^{a,*}, Ioannis Michos^a, Vicky Papadopoulou Lesta^a, Michalis Papadopoulos^a, Evangelos S. Papaefthymiou^a, Andreas Efstathiou^a

^a*School of Sciences, European University Cyprus, Diogenes Street, 6, Engomi, Nicosia, 1516, Cyprus*

Abstract

We present a methodological framework for studying galaxy evolution by utilizing Graph Theory and network analysis tools. We study the evolutionary processes of local ultraluminous infrared galaxies (ULIRGs) and quasars and the underlying physical processes, such as star formation and active galactic nucleus (AGN) activity, through the application of Graph Theoretical analysis tools. We extract, process and analyse mid-infrared spectra of local ($z < 0.4$) ULIRGs and quasars between $5\text{-}38\mu\text{m}$ through internally developed Python routines, in order to generate similarity graphs, with the nodes representing ULIRGs being grouped together based on the similarity of their spectra. Additionally, we extract and compare physical features from the mid-IR spectra, such as the polycyclic aromatic hydrocarbons (PAHs) emission and silicate depth absorption features, as indicators of the presence of star-forming regions and obscuring dust, in order to understand the underlying physical mechanisms of each evolutionary stage of ULIRGs. Our analysis identifies five groups of local ULIRGs based on their mid-IR spectra, which is quite consistent with the well established *fork* classification diagram by providing a higher level classification. We demonstrate how graph clustering algorithms and network analysis tools can be utilized as unsupervised learning techniques for revealing direct or indirect relations between various galaxy properties and evolutionary stages, which provides an alternative methodology to previous works for classification in galaxy evolution. Additionally, our methodology compares the output of several graph clustering algorithms in order to demonstrate the best-performing Graph Theoretical tools for studying galaxy evolution.

Keywords: galaxies: evolution – infrared: galaxies – (galaxies:) quasars: general – galaxies: active – graph theory – clustering algorithms

1. Introduction

1.1. Theoretical framework and Motivation

One of the major fields of study at the forefront of astrophysical research is the study of galaxies in the observable Universe. Ultraluminous infrared galaxies (ULIRGs) are a specific type of galaxies with $1 - 1000\mu\text{m}$ luminosities exceeding $10^{12}L_{\odot}$, discovered by the Infrared Astronomical Satellite (IRAS) in the 1980s (e.g. Soifer et al., 1987; Neugebauer et al., 1984). They have since been the subject of several studies (Sanders et al., 1988; Rowan-Robinson and Efstathiou, 1993; Genzel et al., 1998; Farrah et al., 2003; Imanishi et al., 2007; Veilleux et al., 2009; Farrah et al., 2013). ULIRGs are galaxies undergoing a merger event: when two or more gas-rich disk galaxies interact (Sanders and Mirabel, 1996; Pérez-Torres et al., 2021), they gradually lose their orbital energy and angular momentum, collide with one another and ultimately merge into one larger galaxy. This process (called a *merger*) results in an increase in their luminosity.

The most dominant evolutionary phases of ULIRGs in the merger scenario are the starburst-dominated phase and the AGN-

dominated phase (Efstathiou and Rowan-Robinson, 1995; Genzel et al., 1998; Rigopoulou et al., 1999; Sturm et al., 2000; Spoon et al., 2004, 2007). In this merger scenario, the observed increase in luminosity of these galaxies is caused by the gravitational interaction (and later merger) of two galaxies. During the *pre-merger* phase, this interaction re-distributes stars, as well as the interstellar gas and dust present in each of the galaxies, changing the shape of the galaxies. As this happens, molecular clouds are formed and destroyed, causing new concentrations of interstellar gas and dust which lead to the formation of new active star formation regions within each galaxy. This sudden increase in star formation rate is called the starburst-dominated phase (Efstathiou et al., 2000; Farrah et al., 2001, 2003). The following phase in the merger scenario is called the *coalescence* phase, the intermediate phase where the two galaxies slowly coalesce into one larger galaxy, with a single galactic nucleus (Genzel et al., 1998; Farrah et al., 2003, 2009, 2013). Recent models for galactic mergers have shown that at this stage one or both of the supermassive black holes (SMBHs) at the core of each galaxy display an increase in activity, as they begin to accrete matter. The phenomenon associated with an active SMBH at the center of a galaxy is called an *active galactic nucleus* (AGN). The activation of an AGN is observed as a boost in the AGN fraction of the ULIRG's luminosity, meaning that the fraction of the overall luminosity which is attributed to the

*Corresponding author:

Email address: o.pavlou@euc.ac.cy (Orestis Pavlou)

AGN increases. Finally, the ULIRGs pass into the *post-merger* phase, where the merged galaxy becomes a luminous AGN and the starburst activity drops dramatically. This is caused by the disruption of the feedback process of the SMBH at the core of the galaxy due to increased AGN activity, with galactic winds and highly relativistic jets expelling matter from the core of the galaxy, ‘starving’ the rest of the galaxy of excess dust and gas, while the re-distributed interstellar dust and gas has already been consumed by the starburst phase, during the formation of new stars. The physical processes behind this evolutionary scenario are what we aim to unravel by applying our proposed methodology, using graph theoretical analysis methods and algorithms.

Starburst galaxies display different characteristics than galaxies that go through an AGN-dominated phase. The starburst phase means that a galaxy has an excess of gas and dust, which collapse under gravity to form new stars at a very high rate, whereas the AGN-dominated phase includes the accretion of matter onto the galaxy’s SMBH, which generates large amounts of energy and results in the ejection of gas and dust from the galaxy, via highly energetic jets. Usually this source of energy is obscured by the AGN torus - a dusty toroidal structure surrounding the central SMBH at the center of each galaxy, as predicted by the unified model of AGNs (Antonucci, 1993). This process results in the formation of quasi-stellar objects (QSOs, commonly known as quasars). Quasars are thought to be complementary objects to ULIRGs, but some studies challenge this single evolutionary scenario and suggest the existence of multiple different evolutionary paths to be undertaken by ULIRGs (see Farrah et al., 2003, and references therein). Interestingly, we note that recent studies (Kirkpatrick et al., 2020) detected a population of cold quasars which are not purely AGN objects, as they seem also to be accompanied by strong star formation activity. Strong star formation activity was also inferred in the quasar samples studied by Harris et al. (2016) and Pitchford et al. (2016). The effects of the underlying mechanisms and processes of the merger scenario result in certain differences in the observed characteristics of ULIRGs and quasars. Studying these differences is the key to understanding the evolutionary stages these galaxies go through.

Star formation dominates the far-infrared emission in the spectra of ULIRGs, whereas AGN can make a significant contribution and even dominate the emission of ULIRGs at near- and mid-infrared wavelengths (Farrah et al., 2003; Marshall et al., 2007; Nardini, 2008; Vega et al., 2008; Efstathiou et al., 2022). Extracting the contributions of star formation and AGN activity remains a major challenge. This is mainly due to the presence of dust that hides the energy sources of these galaxies, which results to an absorption of their energetic radiation. Eventually, the absorbed energy is re-emitted as infrared thermal radiation. Understanding local ULIRGs constitutes an important step towards the interpretation of submillimeter galaxies (SMGs) (see Hughes et al., 1998; Barger et al., 1998; Casey et al., 2014) and other populations of galaxies, where extreme starburst and AGN activity occurred in the history of the Universe (e.g. Harris et al., 2016; Pitchford et al., 2016; Rowan-Robinson et al., 2018).

Galaxy spectra, from the ultraviolet to the millimetre (0.1-

1000 μm), encode information about their nature and their evolutionary state. Models for their emission (Efstathiou and Rowan-Robinson, 1995; Silva et al., 1998; Efstathiou et al., 2000; Siebenmorgen and Krugel, E., 2007; Efstathiou and Siebenmorgen, 2009) show that medium resolution spectroscopic data in the 5-35 μm wavelength range are required for determining the properties of galaxies such as uncovering obscured AGN, powered by accretion onto SMBHs and determining the age of the starburst episode. In this work we study the evolution of galaxies by examining mid-infrared spectra of local ultraluminous infrared galaxies and quasars (at $z < 0.4$) with the use of Graph Theory and network analysis.

The observed characteristics in the mid-infrared spectra of galaxies which have been proven to be indicators for the presence of high star formation rate are the emission features of polycyclic aromatic hydrocarbons (PAHs) in specific mid-IR wavelengths (6.2, 7.7, 8.6, 11.2, 12.7 μm), (Roche et al., 1991; Genzel et al., 1998; Peeters et al., 2002). The mid-infrared spectrum also contains information of emission and absorption features around 9.7 and 18 μm caused by the presence of silicate dust. The silicate emission features arise due to the emission of hot dust at a temperature of $\sim 300\text{-}1000\text{K}$ which is viewed almost completely unobscured when the AGN tori are viewed face-on (Rowan-Robinson et al., 1993; Granato and Danese, 1994; Efstathiou and Rowan-Robinson, 1995). The absorption features at 9.7 μm are more difficult to interpret, as they may be either caused by the viewing angle of the torus being edge-on (buried AGN) (Pier and Krolik, 1992; Granato and Danese, 1994; Efstathiou and Rowan-Robinson, 1995; Imanishi et al., 2007) or by obscured star formation (Rowan-Robinson and Efstathiou, 1993).

Murata et al. (2016) studied the relationship between PAH emission and star formation in nearby galaxies at $z < 0.2$, by analyzing data on 55 star-forming galaxies from different instruments (AKARI, WISE, IRAS, Hubble Space Telescope and SDSS) and found that PAHs are partially extinguished during the late stages of galactic mergers. The most likely culprits for this are strong radiation fields and large-scale shocks taking place during mergers. In a separate work by Shipley et al. (2016), the authors study the PAH emission features of galaxies at $1 < z < 3$ to calibrate their star formation rates (SFRs). Using Spitzer (IRS) observations they demonstrate how PAH emissions can accurately describe SFRs in galaxies and thus help distinguish between star-forming and AGN-dominated galaxies. The classification of the evolutionary phase of galaxies via the study of silicate absorption strength and PAH emission in the mid-infrared range was also performed by Spoon et al. (2007). The authors of this work show how the specific emission features of PAHs at 6.2 μm and silicate strength at 9.7 μm can be a useful indicator to distinguish between starburst and AGN dominated galaxies. They present their results graphically in a ‘Fork’ classification diagram.

Recent studies of luminous infrared galaxies have revealed differences in the properties of these galaxies at low vs high redshift. The most luminous (ultraluminous and hyperluminous) infrared galaxies at low redshift are consistent with a galactic merger scenario. However, studies with Herschel (Rodighiero,

G. et al., 2010) discovered the lesser role of starbursts triggered by mergers in the high redshift Universe. The idea that ‘Main Sequence’ galaxies, or galaxies with significant contribution from ‘cirrus’, can reach infrared luminosities exceeding $10^{12}L_{\odot}$ was also suggested pre-Herschel by Efstathiou and Rowan-Robinson (2003) and Efstathiou and Siebenmorgen (2009). Intense obscured starburst and AGN activity triggered by mergers is still considered to be the dominant power source in the most luminous galaxies observed in Herschel surveys (Rowan-Robinson et al., 2018; Gao et al., 2021). Current ideas also suggest that the mergers that occurred in the early Universe may not have been as efficient at triggering starbursts as similar events in the local Universe. Thus, the local merger scenario may not cover the entire sample of observed luminous galaxies in the early Universe (e.g. (Schreiber et al., 2015)).

The more traditional study of spectral energy distributions (SEDs) of galaxies involves fitting their spectra with models which incorporate stellar population synthesis models (Bruzual and Charlot, 1993, 2003) and treat the effects of dust either in a simplified geometry (e.g. in codes like MAGPHYS and CIGALE) or in more detailed treatments like radiative transfer models like GRASIL (Rowan-Robinson and Efstathiou, 1993; Silva et al., 1998; Vega et al., 2008; Efstathiou et al., 2013, 2014, 2021, 2022). In addition, an AGN model is usually included in the fitting and in some cases the AGN can dominate the luminosity. The approach adopted by Farrah et al. (2009) using Graph theory and Bayesian inferencing to study the evolution of 102 local ULIRGs is an alternative to the SED fitting approach and it has the advantage that it can lead to the identification of different phases in the evolution of luminous infrared galaxies and the development of an evolutionary paradigm. Farrah et al. (2009) successfully developed an evolutionary paradigm for low redshift infrared galaxies using this approach.

In this work we analyze data obtained from NASA’s *Spitzer Space Telescope* and in particular the *Infrared Spectrograph (IRS)* instrument onboard that spacecraft. More specifically, we extract, process and compare mid-infrared wavelength (5 – 35 μm) spectra of local ($z < 0.4$) ultraluminous infrared galaxies (ULIRGs) and quasars, in order to generate a relational (similarity) graph of these galaxies and use Graph Theoretical tools to perform network analysis. We use publicly available data provided via the CASSIS website (Combined Atlas of Sources with Spitzer IRS Spectra) of infrared galaxy sources. There are several important samples consisting of hundreds of galaxies (Fu et al., 2010; Sajina et al., 2012; Kirkpatrick et al., 2015, 2020) with publicly available data through the CASSIS database (see Leboutteiller et al. (2011, 2015)). As in the case of the sample studied by Farrah et al. (2009), the samples include mid-infrared data from the Spitzer Space Telescope which are essential for this kind of analysis. This approach is especially useful for studying the evolution of infrared galaxies given the availability of data for large samples of galaxies that are already available (e.g. from projects like HELP Shirley et al. (2019, 2021)) and which will soon be complemented with spectroscopic data from the James Webb Space Telescope (JWST) which was launched by NASA in December 2021.

1.2. Graph Theory in Astrophysics

Graph Theory is the discipline of Mathematics and Computer Science involved with the study of the relations between objects, based on their relational properties, which are extracted from the data into matrices. These matrices are then used to generate and map the objects in a network structure called a *graph*. The objects are presented as *nodes* (vertices) in the graph, and are connected via *edges*, which correspond to their relational properties. One of the major approaches to extract meaningful information from a graph, is the application of *clustering algorithms*, which are unsupervised learning techniques that separate the graph into distinct groups (clusters) of nodes which are more highly connected between them compared to the rest of the graph.

In our specific case, we apply a *similarity function* to the mid-infrared spectra of ULIRGs in order to create a *similarity matrix*. This similarity matrix is then used to generate our graph, which is called a *similarity graph*. In this similarity graph, the nodes represent ULIRGs, which are connected based on the similarity of their mid-infrared spectra. We then apply, test and compare several clustering algorithms, resulting in the detection of communities of ULIRGs with similar spectra.

One of the main advantages of this approach is the fact that it not model-dependent, as the entire process of generating the similarity graph is based purely on the pairwise similarities between nodes obtained by comparing the corresponding observational data. Therefore, the implementation of this methodological approach to astrophysical data, and in particular to the mid-infrared spectra of ULIRGs, is completely independent of any model parameters (compared to model fitting approaches which are heavily dependent on model parameters). Thus, the application of graph theoretical methods for the study of the merger scenario of ULIRGs can produce model-free results, by using the clustering of ULIRGs into similar evolutionary stages based on the similarities between their mid-infrared spectra, in order to generate an evolutionary paradigm for ULIRGs.

Despite the long history of graph theory and its successful implementation in various sciences, there are very few works that exploit Graph Theory in order to study open problems in Astrophysics and specifically galaxy evolution. The only major work that utilized Graph Theory for the study of ULIRG evolution was performed by Farrah et al. (2009). The authors study mid-infrared spectra of a set of Spitzer (IRS) ULIRGs by combining the methods of Graph Theory and Bayesian inferencing in an attempt to identify and distinguish between different phases of temporal evolution. They select a local ($z < 0.4$) ULIRG population and utilize Bayesian inferencing on their mid-infrared spectra to produce a *similarity graph*, where galaxies of similar SEDs are connected to each other in the graph. Then, using a spring-layout (Kobourov, 2012) drawing of the graph (where similar nodes are placed closed in the graph embedding), they identify 3 groups of galaxies which are suggested to correspond to different evolutionary stages of the galaxies.

Although the exploration of graph theory in astrophysics is limited, more research works have been performed in the field

of cosmology. For example, Coutinho et al. (2016) utilized dynamical network analysis of cosmological models of large-scale structures, containing a number of simulated galaxy distributions, in order to study the gravitational interactions and evolution of galaxy clusters and superclusters. Additionally, Hong and Dey (2015) as well as Sabiu et al. (2019) showcased how graph theoretical methods and tools can be successfully applied to simulated as well as observational data. The aforementioned works suggest that the application of Graph Theory can also be a very useful tool in the cosmological study of galaxy formation and distribution.

Finally, the recent papers of Papaefthymiou et al. (2022) and Ioannides et al. (2022) have demonstrated uniform frameworks for performing analysis and classification of ultraluminous infrared galaxies based on Graph Theory and the utilization of graph clustering tools. The applicability of the framework is demonstrated in diverse application domains, which include astrophysical data analysis to study galaxy evolution.

1.3. Methodology overview

In this paper we propose a new classification diagram for ULIRGs and quasars, derived from graph theoretical analysis; in particular graph clustering. This approach enables us to group and classify the spectra of the ULIRG sample of Farrah et al. (2009) along with the spectra of 37 Palomar Green quasars (Symeonidis et al., 2016).

Our methodology consists of three steps: (i) We model the data with a certain type of a weighted graph (a *similarity graph*), in which nodes represent galaxies and edges are weighted based on the similarity of their end-points. More precisely, weights measure the similarity between the SEDs of galaxies. (ii) We apply graph clustering algorithms to identify groups of similar galaxies (clusters) and use well-known graph theoretical measures to validate the clustering. (iii) Finally, we interpret each cluster from an astrophysical point of view, in terms of the physical properties of ULIRGs, such as the PAH emission and silicate absorption features.

The proposed methodology results in a classification scheme that: (a) improves the grouping in Farrah et al. (2009), since it employs the application of graph clustering, and (b) generalizes the popular diagram of Spoon et al. (2007), by viewing the resulting clustering in the PAH emission - Silicate absorption plane.

Roadmap: The paper is organized as follows: In section 2 we describe the observational data we used in our analysis. We use the spectroscopic data obtained with the IRS instrument on-board Spitzer (Houck et al., 2004) which covers the wavelength range $5 - 35\mu\text{m}$ (Lebouteiller et al., 2011). In section 3, in order to be self-contained, we briefly describe the Kernel PCA and graph theoretic methodology we employ. In section 4 we describe our methodology for the construction of the graphs, as well as the graph clustering algorithms' implementation in more detail. In section 5 we present and discuss our results. Finally, in section 6 we present our conclusions.

Throughout this work, we assume a spatially flat Universe, with $H_0 = 70 \text{ km s}^{-1} \text{ Mpc}^{-1}$, $\Omega = 1$, and $\Omega_\Lambda = 0.7$.

2. Data Description

2.1. Observational Data

The sample of Farrah et al. (2009) consists of 102 local ULIRGs with redshifts between $0 < z < 0.4$. The data were acquired by NASA's Spitzer Space Telescope's (Werner et al., 2004) Infrared Spectrograph (IRS) instrument (Houck et al., 2004), which covers the wavelength range between $5 - 35\mu\text{m}$. The spectra were extracted from the *Combined Atlas of Sources with Spitzer IRS Spectra*¹ (CASSIS) website, with ID:105 - *Spectroscopic Study of Distant ULIRGs II* by James R. Houck & Lee Armus. This dataset is comprised of 118 objects observed in Low-Resolution and 53 observed in High-Resolution. Similarly to Farrah et al. (2009), due to the lack of any synchronous sky-background data for the High-Resolution set, we chose to study the Low-Resolution dataset of CASSIS version LR7, released in June 2015 by Lebouteiller et al. (2015), which is a more mature pipeline version of the data than the one used in Farrah et al. (2009), originally presented in Desai et al. (2007).

Palomar Green (PG) quasar spectra were added to our sample, taken from Symeonidis et al. (2016), in order to create a more complete total sample of local ULIRGs and quasars. Due to the limited number of quasars present in the previous sample (in Farrah et al. (2009)), we decided to make this addition to generate a more significant sample of quasars within our total sample. This was necessary in order to eliminate any potential sample bias caused by the much higher number of ULIRGs in other evolutionary phases (i.e. starburst-dominated) influencing the clustering analysis of our similarity graph. We were able to extract IRS spectra from the CASSIS website for 58 PG quasars. Due to the fact that some of these quasars were only observed between $14 - 37\mu\text{m}$, a spectral region that excludes the range of interest studied in this work, namely certain PAH emission and silicate features, we had to limit our sample size to 42 quasars. By cross-referencing this sample with the ULIRG sample of Farrah et al. (2009), we were able to add 37 of the aforementioned PG quasars, with redshifts between $0 < z < 0.2$ to the ULIRG sample, bringing our total sample size to 139 ULIRGs and PG quasars.

2.2. Data pre-processing

The data pre-processing was accomplished completely via our own purpose-made Python code for extracting and pre-processing the aforementioned data². Firstly, we extracted,

¹The data is publicly available at the CASSIS website: <https://cassis.sirtf.com/>

²Our purpose-developed Python code for feature extraction, processing routines and application of our graph theoretical analysis and algorithms are available in a public Github repository.

cross-referenced and corrected the redshift values of each galaxy using the *NASA/IPAC Extragalactic Database (NED)*³. After filtering the spectra to remove possible double flux values, caused by overlapping orders between the Short-Low (SL) and Long-Low (LL) modules of the instrument for specific wavelengths (Houck et al., 2004), we calculated the rest wavelengths: $\lambda_{rest} = \frac{\lambda_{obs}}{1+z}$ and interpolated flux densities per rest wavelength bin, between $5.5 - 26.0\mu m$.

The next steps of our Python pre-processing routines involve continuum fitting to the data to remove the continuum from the observed signal, in order to estimate more accurately certain important physical features present in infrared (rest) wavelengths between $6.2 - 12.7\mu m$. In this wavelength range, we calculate the emission signals of polycyclic aromatic hydrocarbons (PAH) at $6.2, 7.7, 8.6, 11.2$ and $12.7\mu m$ and the absorption/emission feature of silicate dust particles at $9.7\mu m$.

2.3. Feature extraction

As mentioned previously, these PAH features are indicators of the rate of star formation activity in a galaxy. As their name suggests, they are chemical compounds made up of hydrogen and carbon atoms and they have been shown to be abundant in cold molecular clouds (Lebouteiller et al., 2011). These molecular clouds have been extensively studied in several galaxies, and are mostly present in regions of active star formation (also referred to as ‘stellar nurseries’), where young stars form at an increased rate compared to the rest of the galaxy.

For the calculation of the PAH equivalent width, we wrote our own Python routine which interpolates the flux values at each PAH wavelength (i.e. $6.2\mu m$) and then makes use of *scipy*’s *InterpolatedUnivariateSpline*⁴, in order to integrate between values $\pm 0.3\mu m$ around each wavelength (i.e. between $5.9\mu m - 6.5\mu m$ for the $6.2\mu m$ PAH feature). We then use this integral result (F_λ) to calculate the equivalent width (W_λ) as:

$$W_\lambda = \int (1 - F_\lambda/F_c) d\lambda$$

where F_c denotes the flux of the continuum, estimated by using the flux values $\pm 0.3\mu m$ around each PAH wavelength.

For example, the calculation used for the $6.2\mu m$ PAH feature will be:

$$W_{6.2} = \int_{5.9}^{6.5} (1 - F_{6.2}/F_{5.9-6.5}) (0.6)$$

Similarly, as mentioned previously, the *silicate feature* at $9.7\mu m$ has been linked to the presence of silicate dust in the line-of-sight between the observer and the AGN in the core of

ULIRGs, mainly in an area around the AGN called the *torus*. Silicate dust can exhibit either an emission or an absorption feature, unlike PAHs. For the calculation of the silicate feature strength, we use the *specutils* tools⁵ of the *Astropy* Python package, to create a spectrum from the flux density, perform continuum fitting using the *Chebyshev1D* model and the *LinearLSQFitter* module and then divide the flux over the fitted continuum. This is a necessary step before calculating the silicate feature strength, as the feature is quite broad and is prone to the distortions of the spectrum, due to continuum differences between ULIRGs. This is a similar technique to the one used by Spoon et al. (2007).

The silicate absorption/emission feature strength calculation formula is:

$$Si = \log\left(\frac{F_{obs}}{F_{cont}}\right)$$

where F_{obs} = observed flux at $9.7\mu m$ and F_{cont} = continuum flux at $9.7\mu m$.

The calculated PAH emission equivalent widths for $6.2\mu m$ and $11.2\mu m$ and the silicate absorption strengths at $9.7\mu m$ based on the aforementioned methodology implemented in our work are presented in Table A.2 in Appendix D. It is worth noting that these results show some level of consistency compared to the corresponding values presented in other works (e.g. Desai et al. (2007), Spoon et al. (2007), Farrah et al. (2009)). There are some deviations in the estimation of these values compared to those works for certain specific cases of ULIRGs, but the overall trend of the data is in agreement with these works. This is apparent when comparing our versions of the *fork* diagrams (shown in Figure 8 of this work) to the fork diagram of Spoon et al. (2007), where most of the ULIRGs are consistently placed within the same regions of the nine diagram regions (1A-3C), as discussed in Section 5.4.1 of this work.

3. Mathematical Framework

In this section we present the graph theoretical framework that is utilized in this work, which includes the similarity functions and graphs and graph clustering algorithms and quality measurements.

3.1. Graph Theory Background

Graph Theory, one of the oldest branches of Mathematics, is undeniably one of the most powerful tools of Applied Mathematics with remarkable interdisciplinary applicability in diverse areas, spanning from Social and Political Sciences, to Biology, Chemistry, Neuroscience (Bullmore and Sporns, 2009) and Astrophysics and Cosmology (Ueda, H. et al., 2003; Farrah et al.,

³NASA/IPAC Extragalactic Database (NED) website: <https://ned.ipac.caltech.edu/>

⁴Scipy - Interpolated Univariate Spline tool: <https://docs.scipy.org/doc/scipy/reference/generated/scipy.interpolate.InterpolatedUnivariateSpline.html>

⁵Specutils tool (Astropy) documentation: <https://specutils.readthedocs.io/en/stable/>

2009; Hong et al., 2016) and stands out as a foundational concept of Network Science (Barabási and Pósfai, 2016).

Graphs are mathematical structures that represent any type of entities which can be related to each other via pairwise relations. Each entity is represented by a vertex (node) of the graph. Pairwise relations between entities are represented via edges (links) connecting pairs of corresponding nodes. Additionally, a numerical value (weight) can be associated with each edge, which acts as an indicator of the strength of the relation between the corresponding nodes. For similarity graphs in particular, weights quantify the degree of *similarity* between the endpoints of their edges (Blondel et al., 2004).

More formally, an un-directed, weighted and loop-less *graph* G is an ordered triple $G = G(V, E, w)$, where $V = [n] = \{1, 2, \dots, n\}$ is the vertex (or nodes) set; $E \subseteq \{(i, j) : i, j \in V, i \neq j\}$ is the edge set; and w is a *weight function* $w : E \rightarrow \mathbb{R}^+$, specifying a positive *weight* $w(i, j)$ for each edge $(i, j) \in E$. For any fixed vertex $i \in V$, the (*weighted*) *degree* of i is defined as $\deg_i \equiv \sum_{(i,j) \in E} w(i, j)$. The *degree vector* of G is the column vector $\mathbf{deg} = (\deg_1, \dots, \deg_n)^T$ and the corresponding *degree matrix* of G , is the diagonal matrix $\mathbf{D} = \text{Diag}(\deg_1, \dots, \deg_n)$.

A concise way to represent G is through its (*weighted*) *adjacency matrix*: an $n \times n$ matrix $\mathbf{A} = (a_{ij})$, where $a_{ij} \equiv w(i, j)$, for each $(i, j) \in E$ and $a_{ij} \equiv 0$ otherwise. Note that for un-directed graphs, the adjacency matrix is *symmetric*, and consequently all its eigenvalues are real numbers.

Another useful matrix is the (*discrete*) *Laplacian matrix*, which - when viewed as a linear operator - is a discrete analogue of the Laplace operator $\Delta f = \nabla^2 f$ of a real-valued function f . It relates to many useful geometric properties of a graph and is defined as $\mathbf{L} \equiv \mathbf{D} - \mathbf{A}$. To be able to compare such properties among graphs of varying order, one has to consider certain normalized versions of \mathbf{L} , since \mathbf{L} is un-normalized. The most common ones in the literature are: the *normalized symmetric Laplacian* $\mathbf{L}_{sym} \equiv \mathbf{D}^{-1/2} \mathbf{L} \mathbf{D}^{-1/2}$ and the *normalized random walk Laplacian* $\mathbf{L}_{rw} \equiv \mathbf{D}^{-1} \mathbf{L}$. All versions of the Laplacian are symmetric and *positive semi-definite* matrices, hence their eigenvalues are real non-negative numbers. Furthermore, the eigenvalues of the normalized Laplacians are bounded in the interval $[0, 2]$, regardless of the order of the graph into consideration.

Graph Properties: For any $S \subseteq V$, we denote by \bar{S} its complement $V \setminus S$ in V . Two vertices $i, j \in V$ are considered *neighbours* if there is an edge connecting them, i.e. $(i, j) \in E$. The *Volume* of $S \subseteq V$ is the sum of the degrees of its vertices, i.e., $\text{Vol}(S) \equiv \sum_{i \in S} \deg_i$. We also define the volume of the whole graph to be $\text{Vol}(G) \equiv \text{Vol}(V)$. If e is the sum of all weights of the edges of G , then clearly $\text{Vol}(G) = 2e$. A *path* in G is a sequence of nodes $\{v_1, \dots, v_i, v_{i+1}, \dots, v_k\}$ such that $(v_i, v_{i+1}) \in E$. A graph is *connected* if there is at least one path between any pair of vertices. A graph G , in which $\forall i, j \in V$, it holds that $(i, j) \in E$, is called a *complete graph*. A graph $G' = (V', E')$ is a sub-graph of a graph $G = (V, E)$ if $V' \subseteq V$

and $E' \subseteq E$. If G' contains all edges that join vertices V' in G , we say that G' is an induced sub-graph of G .

3.2. Similarity Functions and Similarity Graphs

A *similarity function* (*similarity measure*) s is a function that uses information from entities i, j and yields a real valued number $s(i, j)$, with large values corresponding to high degree of similarity. Quantifying the similarity between all pairs of n entities in a data set results in an $n \times n$ matrix, the *similarity matrix* $\mathbf{S} = (s_{ij})$, with $s_{ij} = s(i, j)$. A specific similarity matrix \mathbf{S} can be used as the adjacency matrix of a graph. The graph is weighted, with the weight function being the similarity function s ; un-directed, since $s(i, j) = s(j, i)$; and loop-less, after assigning 0 to all diagonal elements of \mathbf{S} . The corresponding graph is called *similarity graph* and its adjacency matrix is called *similarity matrix*. For the purposes of this work, we only consider similarity graphs.

Most similarity functions use a distance metric (e.g. Euclidean distance) to compare different data-points. It's clear that such metrics actually quantify the dissimilarity rather than the similarity of the data. Turning dissimilarity into similarity can be done in different ways (e.g. negating, taking the inverse or using a negative exponent of a distance measure). One of the most popular choices, which is used throughout this work, is the *Gaussian kernel function*, commonly used in spectral graph clustering. A more detailed presentation of the Gaussian kernel function is presented in Section 4.1.

3.3. The Graph Clustering Problem and its Quality measures

Clustering constitutes a fundamental problem in sciences: given a set (or system) of (any) discrete simple or structural data, we need to create a much smaller set (than the size of the actual data set) of groups of data, where each data point belongs to one of these groups and the data assigned to the same group have some significant relation (e.g. commonalities, dependencies) to each other. Given a graph, the *graph clustering* problem concerns the task of partitioning the nodes of the graph into groups, called *clusters* or *communities*, such that the nodes within each group are highly connected to each other and while the inter-crossing connections between nodes of different groups are as few as possible (Fortunato, 2010). Communities indicate groups of nodes of the graph which are highly related to each other according to the modeling of the system through a graph. In this work, we consider similarity graphs. A clustering in such a graph reveals partitioning of the nodes of the graph into nodes of similar properties, under the similarity property captured by the edges of the graph. Although, there is no universal definition for the graph clustering problem, a general, informal definition of graph clustering is the following:

Definition 3.1. A *graph clustering* of a weighted graph defined as $G(V, E, w)$ is a partition $C = \{C_1, \dots, C_r\}$ of the vertex set V into r *clusters* or *communities*, for some $r \in \mathbb{N}$, i.e., $C_i \subset V$, $C_i \cap C_j = \emptyset$, for all $C_i, C_j \in C$ and $\bigcup_{i=1}^r C_i = V$, such that the

vertices within each cluster should be highly connected to each other, while the inter-crossing connections between vertices of different clusters should be as few as possible.

3.3.1. Quality measures of Graph clustering

For a weighted graph G and a subset $S \subseteq V$, let $e_{in}(S)$ denote the sum of the weights of all edges joining internal vertices of S , and $e_{out}(S)$ denote the sum of the weights of all edges with one vertex in S and the other vertex in \bar{S} . Set also $e(S) = e_{in}(S) + e_{out}(S)$ and $e = e(V)$, when $S = V$. Note that clearly $vol(S) = 2e(S)$.

Using these notions we can express graph clustering as an optimization problem of computing a graph partition C in which for each cluster $C \in C$, the ratio $\frac{e_{in}(C)}{e_{out}(C)}$ is as large as possible. The following two notions (modularity and conductance) are quantitative measures for the performance of the graph clustering.

Modularity The most known measure of a good graph clustering C is the notion of *modularity* which was first introduced by Girvan and Newman (2002). The modularity m_C measures the fraction of the edges that fall within clusters minus the expected number in an equivalent network, where edges were distributed at random, while the expected degree of the vertices is the same as the original graph. More formally: $m_C \equiv \frac{1}{2e} \sum_{i,j \in V} \left(w_{ij} - \frac{\deg_i \deg_j}{2e} \right) \delta(C_i, C_j)$, where δ is the *Kronecker delta function*, which in our case means that $\delta(C_i, C_j) = 1$ when the vertex j lies in the cluster C_i and $\delta(C_i, C_j) = 0$, otherwise. One can confirm that $m_C \in [-1/2, 1)$. Given a larger than expected portion of connections within a cluster, one can infer the presence of an underlying cluster structure. Finding a graph partition that maximizes modularity is considered NP-complete (Brandes et al., 2008).

Graph Conductance

Let G be a connected weighted graph of n vertices. For a subset $S \subseteq V$, the *conductance* of S is defined as $\phi(S) \equiv \frac{e_{out}(S)}{e(S)}$. Since clearly $\phi(S) \in [0, 1]$, the conductance may be viewed as a probability measure, e.g., if $\phi(S) = 0.1$ it means that 90% the neighbors of a random vertex in S are expected to be in S .

The conductance of a clustering of $r \geq 2$ clusters (or r -way clustering) $C = \{C_1, \dots, C_i, \dots, C_r\}$ is then defined to be the maximum (worst) of all the corresponding conductances of the clusters $C_i \in C$. The optimal r -way *conductance* for the graph G is then defined as the minimum of the conductances of all possible r -way clusterings C of G .

3.3.2. Graph Clustering Algorithms

Graph clustering algorithms are essentially unsupervised learning techniques for the detection of communities (clusters) within a graph. There is an extensive literature on graph clustering algorithms with a multitude of approaches for the computation of clusters in graphs: hierarchically (Lian et al.,

2007), agglomeratively (Newman, 2004) or by divisive methods (e.g. Girvan and Newman (2002); Newman and Girvan (2004)), driven by various measurements of clustering quality (e.g. modularity based Newman and Girvan (2004); Blondel et al. (2008a)), using various graph properties, such as edges or cycles (e.g. Radicchi et al. (2004)), utilizing spectral graph theory and eigenvectors (e.g., (Newman, 2006; Shi and Malik, 2000)), or ones that combine the aforementioned approaches.

In this work we explore two of these important research approaches: (1) Graph clustering algorithms applied directly on the similarity graph, which utilize modularity or conductance as a quality measure, and (2) spectral graph clustering algorithms that utilize eigenvectors for performing the clustering and conductance to measure the quality of the clusters obtained.

Within the first class of algorithms we explore (i.e. modularity-based algorithms), we investigate two of the most popular *hierarchical agglomerative* algorithms: The Leiden algorithm of Traag et al. (2019), which is an improved version of the Louvain algorithm of Blondel et al. (2008a), and the Walktrap algorithm of Pons and Latapy (2006). *Hierarchical agglomerative* clustering algorithms detect network communities by building a hierarchy of clusters, starting from each node being a cluster on its own and progressively merging pairs of clusters until only one final cluster containing all nodes in the network is achieved, by trying to maximize the quality of the obtained clusters. Both algorithms explored in this work utilize modularity to find optimized clusters, as we explain below. Additionally, we also implement the Walktrap algorithm which uses conductance as an optimization measure.

The Louvain algorithm applies a greedy step approach in order to maximize the modularity of the clustering being constructed. First, small communities are found by optimizing modularity through one-node alternations between neighbouring communities, until no further improvement of modularity is possible. Then each small community is grouped into one node and the first step is repeated. Here, we also apply the Leiden algorithm of Traag et al. (2019), which was suggested as an improvement of the Louvain algorithm, that yields communities that are guaranteed to be connected. The Leiden and Louvain algorithms are two of the most popular algorithms for community detection due to the fact that they perform very well in practice, both in terms of time efficiency and quality of the communities detected.

The Walktrap algorithm of Pons and Latapy (2006) is a hierarchical clustering algorithm based on random walks. The algorithm uses the notion of random walks to measure the similarity between two vertices, exploiting the observation that "random walks on a graph tend to get "trapped" into densely connected parts corresponding to communities" (Pons and Latapy, 2006). The corresponding *distance measure* matrix obtained, is then iteratively used for aggregating nodes (and groups) of nodes into clusters trying to maximize a clustering quality measure (e.g. modularity or conductance). A clustering of optimal quality (in the level of aggregation) is returned.

The second kind of graph clustering algorithms we explore

for this work are spectral graph clustering algorithms. These algorithms use the spectrum (eigenvalues and eigenvectors) on a similarity matrix (associated with a similarity graph), or certain matrices derived from it, in order to detect the communities of the associated graph. In particular, spectral clustering algorithms utilize the eigenvalues and eigenvectors of various versions of the Laplacian of the similarity matrix of the graph, to perform dimensionality reduction of the data space in fewer dimensions, before performing the clustering. On this reduced dimension matrix, a standard clustering method is then applied; typically the *k-means* clustering (MacQueen et al., 1967). The spectral clustering algorithms’ main advantage is that clusters are not assumed to be of any specific shape or distribution, in contrast to e.g. a simple k-means algorithm. This means that the spectral clustering algorithms can perform well with a wide variety of shapes of data. On the other hand, the main disadvantage of spectral graph clustering algorithms is that generally they require the number of clusters as an input parameter (although there is a heuristic applied for determining this number).

Spectral clustering algorithms may present some difficulties in identifying communities and distinguishing between clusters in a graph, when dealing with datasets with very close (similar) eigenvalues. Therefore, a better approach is to normalize the data before extracting the eigenvalues and eigenvectors from the similarity matrix. As such, we implement the normalized spectral clustering method proposed by Shi and Malik (2000), and by Ng et al. (2001).

The algorithm of Shi and Malik (2000) involves the following steps: (1) the construction of the similarity or *affinity* matrix using the Gaussian similarity function:

$$A_{ij} = \exp(-\|s_i - s_j\|^2 / 2\sigma^2)$$

where σ is a scale parameter (see section 4 for more details), (2) the computation of an unnormalized Laplacian matrix, (3) the extraction of its generalized eigenvectors and (4) finally, the application of *k-means* in this eigenvector space for the detection of the clusters. The algorithm of Ng et al. (2001) follows a similar process, but implements a normalization of the Laplacian matrix eigenvectors before applying a *k-means* clustering algorithm to extract the clusters, in an attempt to improve the accuracy and computational efficiency of the algorithm. Our study focuses on the second kind of graph clustering algorithms, since the approach allows a more concrete analysis of the quality of the solution. For this reason, the spectral graph clustering algorithms explored here are described in more detail in the methodology section (4).

4. Methodology

In this section we describe the research methodology employed for this work. The first step of the methodology is the construction of a suitable *similarity* graph based on galaxy SEDs (spectra). This is obtained by a careful choice of a similarity function (i.e. the Gaussian Kernel) as well as a sparsification method to obtain a sparse graph that will allow for an easier extraction of the graph clusters.

The second step of the methodology is a comparative and careful application of graph clustering algorithms on the resulting similarity graph for the detection of communities (clusters) of galaxies with similar SEDs. The third step of our approach is to exploit the visualization provided by the graph modeling in order to extract possible hidden relations between various physical properties of galaxies (i.e. SEDs with other physical properties, such as the presence of polycyclic aromatic hydrocarbon (PAH) molecules and silicate dust grains) but also to suggest possible evolutionary processes for the power sources of ULIRGs. Additionally, the exploitation of diverse graph clustering algorithms serves as a verification tool for the algorithms employed, which also provides multi-scale clustering of the galaxies. The last and perhaps most important step of our approach is the interpretation of our results, obtained by comparing them with results from previous works and the established theoretical framework of ULIRGs and their evolution.

For the graph visualization and implementation of network analysis, we utilize several Python packages, such as the *scikit-learn* and *igraph* packages.

4.1. Construction of the Similarity Graph

We recall that the data set under investigation consists of 139 (denoted by N) ULIRGs and quasars. For each of these galaxies, its mid-IR spectra (of D values) is known, resulting to an $N \times D$ matrix, which will be denoted by \mathbf{X} . Additionally, each galaxy’s spectrum is characterized by the presence of distinct PAH emission features (at $6.2\mu\text{m}$ and $11.2\mu\text{m}$) and a deep Silicate absorption/emission feature at $9.7\mu\text{m}$.

From the $N \times D$ matrix \mathbf{X} containing galaxy SEDs, we construct a corresponding *similarity matrix* utilizing a *similarity function* (see Section 3.3). One of the most commonly used functions - especially for the case of spectral graph clustering - is the *Gaussian Radial Basis Function (RBF) kernel*, also known as *Gaussian kernel*, which is defined as:

$$s(\mathbf{x}_i, \mathbf{x}_j) = \exp(-\gamma\|\mathbf{x}_i - \mathbf{x}_j\|^2), \quad (1)$$

where $\|\mathbf{x}_i - \mathbf{x}_j\|$ is the Euclidean distance between the vectors $\mathbf{x}_i, \mathbf{x}_j \in \mathbb{R}^D$, and $\gamma = 1/2\sigma^2$, where σ is the corresponding standard deviation of the Gaussian distribution. In this way, a *similarity matrix* \mathbf{S} can be constructed, where $S_{ij} = s(\mathbf{x}_i, \mathbf{x}_j)$. We also note that, by definition, the Gaussian Kernel is a similarity function (not a dissimilarity one): The smallest the difference between $\mathbf{x}_i, \mathbf{x}_j$, the largest is their corresponding $s(\mathbf{x}_i, \mathbf{x}_j)$ value. Additionally, we note that the Gaussian kernel function provides a non-linear representation of the data set, through the corresponding similarity distances between them, capturing in this way their non-linear relationships. For the aforementioned reasons, we choose to implement the Gaussian Kernel function for the construction of the similarity matrix and the corresponding graph.

We remark that there exist various suggestions for choosing the parameter σ . A common and natural choice (e.g. Veenstra et al. (2017)) is to consider σ to be the standard deviation of the

sample of the $\frac{N}{2}$ distances $\|\mathbf{x}_i - \mathbf{x}_j\|$. In this work we utilize this way for choosing the value of σ . We have tested several other choices for σ , but have chosen this approach since it has been shown to obtain more natural results for the particular data set under investigation.

From the similarity matrix we can now compute the *similarity graph* (and its corresponding adjacency matrix) $G = (V, E, w)$ as follows: V corresponds to the N galaxies under investigation and for each $i, j \in V$, $w(i, j) = S_{i,j}$. Note that the resulting graph is a weighted but almost complete graph (see 3.1). Such a dense graph makes both the visualization of the similarities of galaxies hard to distinguish and also makes the clustering analysis difficult (von Luxburg, 2007). A common way to overcome this difficulty, used both for graph clustering as well as more generally for various graph-theoretic analyses, is the *graph sparsification*. Through this process, the lightest edges among nodes (corresponding to less significant similarities among galaxies) are removed from the graph. The resulting sparse graph contains the most significant edges among pairs of nodes, representing the most important relations between nodes of the network. In the case of similarity graphs the edges with the largest weights remain while the lightest edges are removed from the graph. Two of the most common sparsification methods used for graph clustering are to apply either a global or a local criterion for choosing which edges are removed: (1) The ϵ -neighbourhood method (von Luxburg, 2007) applies a *global* threshold value for the whole graph for the decision of which edge to be removed, keeping only edges of weight greater than the threshold. (2) On the other hand, in the k -nearest neighbour (k -nn) method (von Luxburg, 2007), for each node of the graph, we keep only the k largest weighted edges incident to it. In this work, we utilize the k -nn method for the graph sparsification, with a careful choice for the value of k , as explained in Section 5. The resulting sparse, weighted similarity graph (obtained by applying the Gaussian Kernel on the galaxy SEDs), after the sparsification process is called *SED similarity graph* and is denoted as $G(V, E, \mathbf{W})$ or simply as G .

After the graph construction and sparsification of the SED similarity graph, we first apply some basic network analysis on the resulting graph, in order to achieve a better understanding of the data set under investigation from a network modeling point of view, by computing important properties of the network, such as node degree and node centrality (see Section 3.1). Then, we proceed to the main step of our graph theoretic analysis, which is the application of graph clustering algorithms, on the obtained similarity graph, in order to detect distinct communities of galaxies with similar spectra. This step is explained in detail in the following section.

4.2. Application of Modularity Based and Spectral Graph Clustering Algorithms

The next step of our analysis is the exploration of different graph clustering algorithms on the resulting SED similarity graph. Since graph clustering algorithms in graphs group together highly connected nodes, these groupings correspond to

galaxies of similar SEDs, which may correspond to different stages of galaxy evolution and could also reveal hidden relations between various physical properties of galaxies (i.e. a comparison between PAH emission and silicate absorption features). We explore two kinds of graph clustering algorithms: modularity-based ones (applied directly on the adjacency matrix) and spectral graph clustering algorithms which apply k -means clustering on the eigenvectors of the Laplacian of the similarity graph. Both methods have been described in Section 3.1.

4.2.1. Applying Modularity-based Clustering Algorithms

We explore the application of two modularity-based algorithms on the SED similarity graph: The Leiden algorithm of Traag et al. (2019) and the Walktrap algorithm of Pons and Latapy (2006) (see Section 3.3). The Leiden algorithm returns the clusters for the level of hierarchy that achieves maximal modularity. The Walktrap algorithm also allows for the possibility to return the clusters obtained for any level of hierarchy. Additionally, the Walktrap algorithm works also by utilizing conductance as a criterion for the merging of the clusters, instead of modularity score. This is quite useful for the choice of the level of hierarchy which results in clusters that achieve both optimal conductance and optimal modularity (see Section 5 for more details).

4.2.2. Applying Spectral Graph Clustering Algorithms

Additionally, we explore spectral graph algorithms on the SED similarity graph obtained. As described in Section 3.3, this type of algorithms apply a k -means (MacQueen et al., 1967) on the matrix obtained by the k most significant eigenvectors of the Laplacian of the similarity graph under investigation.

In particular, we utilize the normalized spectral clustering method proposed by Shi and Malik (2000). This method involves the construction of an *affinity matrix*, which corresponds to the similarity matrix obtained by the application of the Gaussian Kernel similarity function in the raw data, as we explained in section 4.1.

This clustering method also involves the computation of an unnormalized Laplacian matrix and the extraction of its generalized eigenvectors, which represent the detected number of clusters of the graph. The entire process, as implemented in this work is explained in Appendix A.

As explained in Section 4.2, spectral graph clustering algorithms require the number of clusters r to be given *a priori* as part of the input. However, there are several related heuristics that compute this value. The most popular method, which we utilize in this work, is the *eigengap* heuristic (von Luxburg, 2007). According to this method, r is the minimum value for which the difference (gap) between the consecutive Laplacian eigenvalues of the Laplacian of the graph G , $\lambda_{r+1} - \lambda_r$ becomes significantly larger (see Section Appendix A for more details).

This is justified by perturbation arguments from the ideal case of r distinct connected components, where clearly $\lambda_1 = \dots = \lambda_r = 0$ and $\lambda_{r+1} > 0$.

The second normalized spectral clustering method we apply is the one proposed by Ng et al. (2001). The proposed algorithm differs from the algorithm of Shi and Malik (2000) mainly in two points: (i) In step (2), it computes the *normalized Laplacian matrix* instead of the unnormalized Laplacian, which is defined as: $\mathbf{L}^{norm} = \mathbf{D}^{-1/2} \mathbf{L} \mathbf{D}^{-1/2}$ and (ii) Adds an additional step between steps (3) and (4), where the rows of matrix \mathbf{X} are re-normalized in order to have unit length, obtaining matrix \mathbf{Y} : with $Y_{ij} = X_{ij} / (\sum_j X_{ij}^2)^{1/2}$. Then, step (4) applies on matrix \mathbf{Y} instead of \mathbf{X} .

Ng et al. (2001) note that there are many similarities between spectral clustering methods and *Kernel PCA* (KPCA), another method which can be used for clustering analysis. The authors also point out that the main difference between their method and KPCA is the initial normalization of the affinity matrix, which improves the algorithm's performance.

5. Results

In this section we present the results we obtain following the methodology described in previous sections. First, we present the constructed (sparsified) similarity graph based on galaxy mid-IR spectra.

Next, we apply several graph clustering algorithms, as explained in section 3.3 to detect communities of galaxies of similar spectra. Next, we compare in a visualized way the SED communities with other physical properties of the galaxies, such as the PAH emission and the silicate absorption features. The methods explored produce communities that correspond to known stages of ULIRG evolution, suggesting an evolutionary path of their power sources. The placement of the galaxies throughout the generated graph provides a visual representation illustrating the similarities between well-known galaxies, as well as relatively unknown ones, that may be of interest for further investigation. Finally, we present an interpretation of the obtained results, combined with the application of domain knowledge, which can lead to verification and improvements upon previous works, as well as novel suggestions for further understanding galaxy evolution.

5.1. The Similarity Graph and Basic Network Analysis

As explained in previous sections, we first use the raw data (i.e. the SEDs of our sample) for the construction of the *similarity graph*, using the Gaussian Kernel. In section 4.1, we justify our choice for the value of σ as the standard deviation based on the Euclidean distances between the vectors x_i, x_j . Additionally, for the sparsification of the similarity graph, we are interested in maintaining both connectedness and an adequate representation of the original data. For large graphs, connectedness is asymptotically guaranteed if k is chosen to be of the

order of $\log(n)$. For small/medium sized graphs though, as in our case, some exploration is required. In our case and for the k -nn method, we check the connectedness of different graphs resulting from increasing values of k . The graphs for k -nn are connected for $k \geq 3$, but $k = 3$ is too sparse. For the purposes of our work we use exclusively the *mutual k -nn* method, in which the k -nearest neighbors are connected via edges which are undirected, meaning that the k -nn connection is mutual between the nodes. The graphs for mutual k -nn might be disconnected, but for increasing k the size of the largest connected component increases. This growth stabilizes for $k = 6$ with $\sim 91\%$ of the nodes being included to this component, while the rest of the nodes are isolated points. Since the mutual k -nn graph is always a subgraph of the standard k -nn graph we simply choose $k = 6$ for the standard k -nn graph.

A drawing of the resulting sparsified graph (in a two dimensional space) is shown Figure 1. The nodes in this figure (and all of the subsequent figures in this work) are referenced with numerical labels as presented in Table A.1 of Appendix C. For the drawing, we use the force-directed layout the Fruchterman-Reingold Algorithm (Fruchterman and Reingold, 1991). Force-directed layout algorithms (Kobourov, 2012) produce graph drawings (layouts) of as few crossing edges as possible, by assigning repulsive forces between all nodes and attractive forces between connected nodes, so that neighbouring nodes are placed closely in the plane.

After the construction of the similarity graph, we first apply some basic network analysis in order to understand the system properties. In particular, we compute the following (global) network properties: (i) network diameter, (ii) average, min max vertex degrees and (iii) network clustering coefficient (which measures how well the neighbours of a node are neighbors to each other). The values of these parameters for the constructed network are shown under Figure 1. We observe that the network demonstrates the following properties: (i) Network diameter = 13, (ii) Average vertex degree = 9.3, (iii) Minimum vertex degree = 7, (iv) Maximum vertex degree = 18 and (v) Network clustering coefficient = 0.52.

The network diameter indicates that the maximum number of shortest paths between connected nodes in the graph is 13. The vertex degree of a graph represents the number of connections to each node. Our graph shows an average degree for each node = 9.3, with the minimum and maximum number of connections being 7 and 18, respectively. The calculated network clustering coefficient (0.52) demonstrates that around half the neighbors are connected to each vertex in the graph (with a value of 0 indicating that no neighbors are connected and a value of 1 indicating that all neighbors are connected to each vertex).

To better understand these results, we can compare them to the corresponding metrics produced by a random graph. For this purpose we have calculated the corresponding metrics of a random graph generated based on the Erdos-Renyi stochastic model. For this implementation we only provide the same number of nodes (139) and number of total edges (834) as produced during the generation of our similarity graph. This results in

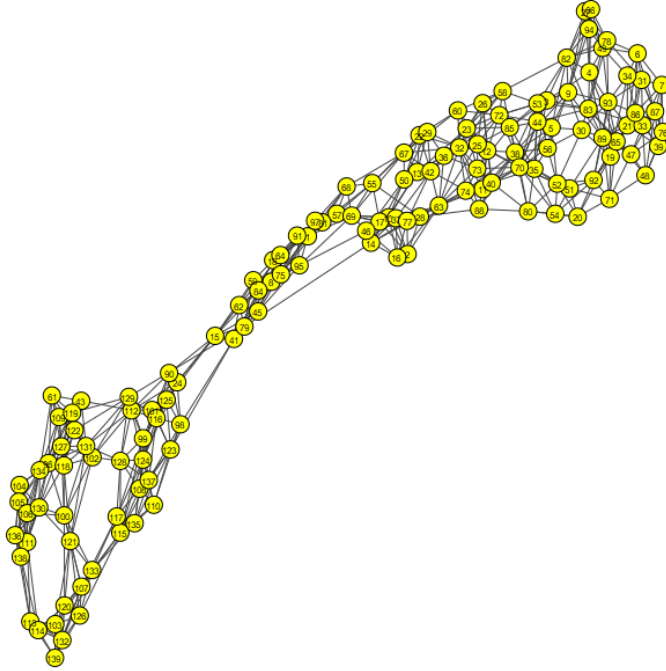


Figure 1: A drawing of the resulting (sparsified) similarity graph using the Gaussian Kernel as a similarity function and the weighted Fruchterman-Reingold spring layout algorithm of igraph for its drawing. The nodes are referenced with numerical labels as presented in Table A.1 of Appendix C. The network demonstrates a *network diameter* = 13, an *average vertex degree* = 9.3, a *minimum vertex degree* = 7, a *maximum vertex degree* = 18 and a *network clustering coefficient* = 0.52.

a network diameter = 3 for the random graph, which is much lower than the network diameter of our similarity graph (= 13), suggesting that a random graph would result in a much more connected network, as expected. This showcases that the nodes in our similarity graph are more widely separated, suggesting a more meaningful structure of the network (with similar nodes being placed much closer together compared to dissimilar ones). Furthermore, whereas the minimum and maximum vertex degrees of the random graph (= 6 and = 20 respectively) showcase similar values to our similarity graph, the average vertex degree of the random graph is = 12, which further indicates a more highly connected network compared to our similarity graph, where the average vertex degree is = 9.3. Finally, the network clustering coefficient of the Erdos-Renyi random graph is = 0.09, a much lower value than that of our similarity graph (= 0.52) which showcases that the neighboring nodes of the random graph are not as well connected as in our similarity graph.

5.2. Extraction of SED Communities

We next apply graph clustering on the SED similarity graph, to identify groups of galaxies with similar spectra. In the following figures we present the results obtained by applying several graph clustering algorithms, as described in Section 4.2. In all of the following graph drawings, different clusters detected are represented with a different color in the corresponding node.

We begin by presenting the results obtained with the implementation of Modularity based algorithms. Figure 2a shows the result obtained by applying the Leiden algorithm of Traag

et al. (2019). Six communities were detected, with an optimal modularity score of 0.7 and a conductance score of 0.30. This result was achieved via the igraph implementation of the algorithm, using a resolution parameter of 1.0 (the resolution parameter determines the granularity of the clustering; a higher resolution parameter corresponds to a lower number of detected communities). We tested several values for the associated resolution parameter. The chosen value achieves the best results, in terms of both the quality of the communities detected as well as their physical meaning. The second Modularity based algorithm explored is the Walktrap algorithm of Pons and Latapy (2006). The result obtained by the application of this algorithm on our graph is shown in Figure 2b. Again, six communities were detected, with a modularity score of 0.7. Furthermore, the algorithm achieves a conductance score of 0.21.

Next, we present the results obtained applying spectral graph clustering algorithms, as explained in Section 4.2.1. Spectral graph clustering algorithms require the number of clusters to be provided as part of the input. Applying the eigengap heuristic shown in Figure 4, the number of clusters r is chosen to be $r = 5$. Based on the methodology explained in section 4.2.1, in order to determine this value, we determine that the minimum value which combines (i) the spectral gap heuristics and (ii) also achieves both the optimal modularity and conductance scores is the value of 5. Hence we choose this value as input for the spectral algorithms explored in our work.

Figure 3a shows the five communities detected by applying the algorithm of Ng et al. (2001) and figure 3b shows the five communities detected by applying the algorithm of Shi

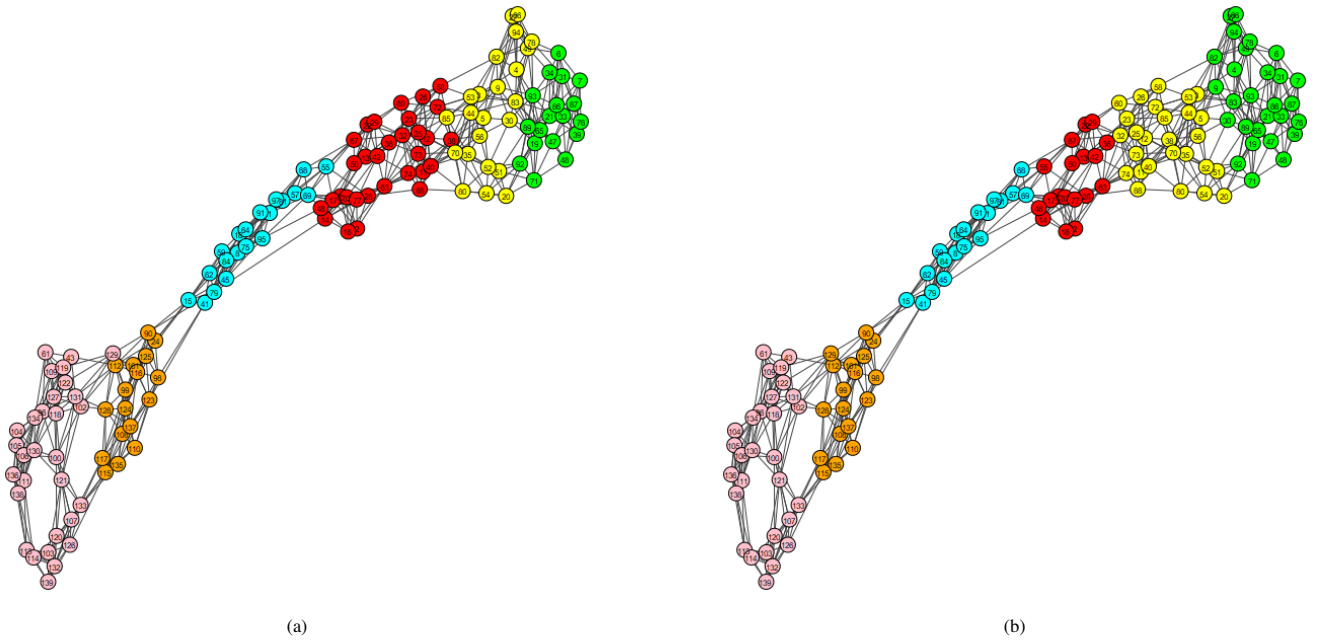


Figure 2: The application of Modularity based algorithms (Leiden and Walktrap) results to the detection of six Communities of very similar quality. (a) Left: Communities detected by applying the Leiden algorithm of Traag et al. (2019) on the resulting similarity graph. The algorithm detected 6 communities and achieved a modularity score of 0.7 and conductance of 0.30. (b) Right: Communities detected by applying the Walktrap algorithm of Pons and Latapy (2006) on the similarity graph. After 30 steps (iterations of hierarchy levels), this algorithm detected 6 communities, with a modularity score of 0.7 and a max conductance of 0.21.

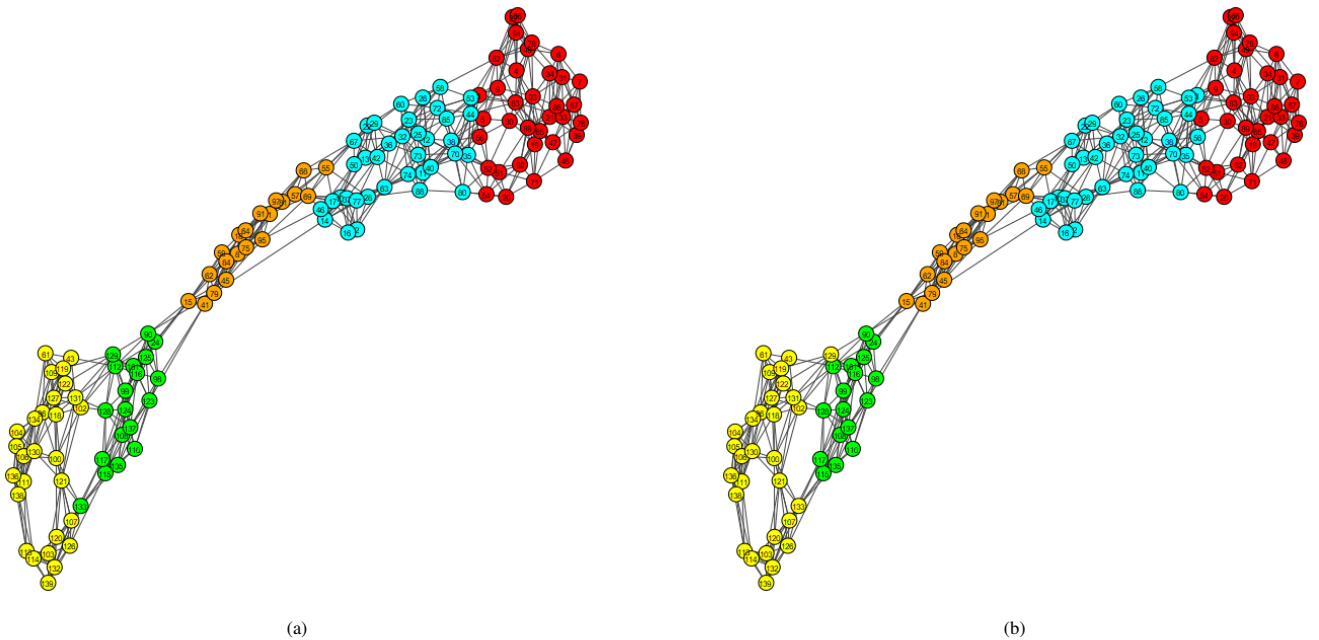


Figure 3: The application of Spectral graph clustering algorithms (Ng & Jordan and Shi & Malik) which results in the detection of five Communities of very similar quality. (a) Left: Communities detected by the spectral graph clustering algorithm of Andrew Ng & Jordan (Ng et al., 2001), by setting the parameter of the number of clusters to be returned to 5. The conductance obtained is 0.05, with a modularity score = 0.68. (b) Right: Communities detected by the spectral graph clustering algorithm of Shi and Malik (2000), by setting the parameter of the number of clusters to be returned to 5. The conductance obtained is 0.05, with a modularity score = 0.68.

and Malik (2000). Interestingly, both algorithms achieve similar conductance values of 0.05, which is much lower than the corresponding values achieved by modularity based algorithms (between 0.2 – 0.3).

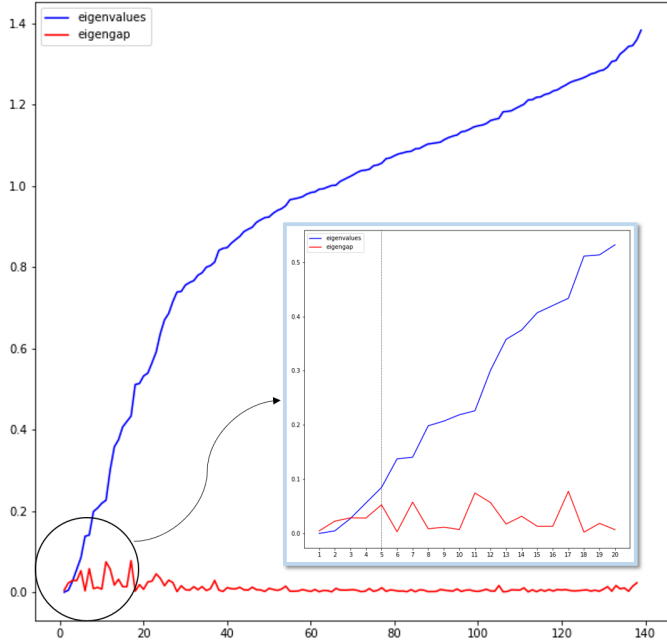


Figure 4: The eigenvalues λ_i of the generalized eigen-problem $\mathbf{L}u = \lambda_i u$ for the unnormalized Laplacian (blue) and the corresponding eigengaps (red). Applying the eigengap heuristic on the smallest 20 Laplacian eigenvalues, the significant gap is found between λ_5 and λ_6 , hence we have $r = 5$ clusters.

5.2.1. Comparing Communities detected by various algorithms

In the previous section we show a qualitative comparison of the outputs of the application of several graph clustering algorithms on our dataset, in which all graph clustering algorithms obtain very similar results visually. In this section, we present a quantitative analysis for comparing these outputs. In particular we would like, for each pair of the algorithms tested, to (i) match the communities detected between the two and (ii) after the mapping of corresponding communities between the outputs of the two algorithms, compute the percentage of nodes that are common in both of the outputs.

ALGORITHM	Louvain	Girvan-Newman	Leiden	Newman	Walktrap	Andrew Ng	Shi & Malik
Louvain	1.000	0.954	0.874	0.843	0.920	0.874	0.924
Girvan-Newman	0.954	1.000	0.847	0.875	0.921	0.869	0.883
Leiden	0.874	0.847	1.000	0.769	0.823	0.892	0.908
Newman	0.843	0.875	0.769	1.000	0.891	0.814	0.795
Walktrap	0.920	0.921	0.823	0.891	1.000	0.839	0.849
Andrew Ng	0.874	0.869	0.892	0.814	0.839	1.000	0.933
Shi & Malik	0.924	0.883	0.908	0.795	0.849	0.933	1.000

Table 1: A pairwise comparison of the graph clustering algorithms explored in this work showing the percentage of common nodes between (corresponding) detected clusters.

Table 1 shows the results of this comparison. We observe a very high percentage of matching of detected clusters be-

tween different clustering algorithms, with an average matching percentage between all algorithms = 86.6%. This means that an average of 120 galaxies of our sample of 139 galaxies are placed in similar communities under all clustering algorithms considered in this work.

The matching percentage between modularity-based clustering algorithms is = 87.6%, with the lowest matching percentage being = 78.7% (between the Leiden and Newman algorithms). The matching percentage between the two spectral graph clustering algorithms of Ng et al. (2001) and Shi and Malik (2000) is = 93.3%. This concludes that the implementation of the different types of clustering algorithms in our graph results in very similar results of detected clusters, especially considering that the optimal number of clusters for modularity-based algorithms (6 clusters) is different than the optimal number of clusters for spectral graph clustering algorithms (5 clusters). We are therefore highly confident on the consistency and nature of the detected communities based on our methodology.

Another interesting observation is the high matching correlation (93.3%) between the clusters obtained by the application of spectral graph clustering algorithms. This means that 130 of the 139 galaxies investigated in this work are placed in matching communities under different spectral graph clustering algorithms.

These results serve as a verification of the validity of the graph clustering algorithms investigated, as well as a demonstration on the suitability of graph theory for investigating similar problems in galaxy evolution and astrophysics.

It should be noted at this point that the difference in the number of detected clusters between the modularity-based algorithms and the spectral graph clustering algorithms arises due to the difference in the methodology of these two distinct types of clustering algorithms. The modularity-based algorithms consistently detected six clusters, based on the optimization of the modularity score in each implementation. Comparatively, as mentioned previously, the spectral graph clustering algorithms take the number of detected clusters as a parameter for their implementation. In this case, we use a purely mathematical justification for determining the appropriate number of clusters, based on the Laplacian eigengap heuristic (von Luxburg (2007)) method presented in Figure 4. Using this mathematical justification for the selection of the number of clusters, we observe an improved clustering performance by the spectral graph clustering algorithms compared to the modularity-based algorithms, as is evident by the resulting maximum conductance scores of each algorithm, which is much lower in the case of the former (0.05) compared to the latter (0.2 – 0.3). This result represents a quantitative demonstration of the improved clustering performance for the case of the spectral graph clustering algorithms on our similarity graph.

Based on these results, we have chosen to further investigate the physical features of our sample in following sections using the communities detected by the implementation of the Shi and Malik (2000) algorithm for the purposes of this work. The communities detected from the implementation of the clustering

algorithms considered in this work are presented in Appendix B.

5.3. Astrophysical Interpretation of Communities

In this section, the graph drawing of the network modeling of the set of galaxies under investigation is explored, in order to first relate the communities detected with physical properties of the galaxies (i.e. PAH emission and silicate absorption features) and secondly to relate and compare the graph theoretical classification obtained in this work with other classification methods, and in particular the well known galaxy classification *fork* diagram introduced by Spoon et al. (2007).

The graphs in Figures 3a and 3b present the clusters detected using the Spectral Graph Clustering algorithms of Ng et al. (2001) and Shi and Malik (2000), respectively, using a preset number of clusters = 5. As mentioned previously, the implementation of these algorithms result in the detection of similar communities (93.3% match). Two communities of mostly starburst-dominated ULIRGs and two communities of mostly AGN-dominated quasars are identified, as well as one community of ULIRGs dominated by both starburst and AGN emission, which can be interpreted as a transitional phase between the distinct starburst and AGN-dominated phases.

In Figure 5 we plot the calculated mean interpolated signals (flux density over rest wavelength) of each cluster identified by the Shi and Malik (2000) algorithm. The signals were normalized at $14\mu\text{m}$, in order to directly compare the signals' features. Additionally, we display certain features of the mid-IR spectra of ULIRGs for each cluster in the legend of Figure 5, such as the mean IR luminosity (scaled as $\log_{10}(L_{\text{IR}}/L_{\odot})$), the mean starburst luminosity (in units of $10^{12}L_{\odot}$) obtained from Efstathiou et al. (2022), the mean AGN luminosity (in units of $10^{12}L_{\odot}$) obtained from Efstathiou et al. (2022), the calculated mean PAH equivalent width values at $6.2\mu\text{m}$ and $11.2\mu\text{m}$, as well as the estimated mean silicate absorption strength at $9.7\mu\text{m}$ (Si 9.7). These mean signals, as well as the aforementioned mean features of each cluster suggest that the clustering algorithms managed to recover the known optical spectral types of the galaxies, namely H_{II} galaxies, the low-ionization nuclear emission-line regions (LINERs), as well as the Seyfert-2 galaxies and a combination of Seyfert-1 galaxies and luminous quasars (e.g. Kewley et al., 2006; Imanishi et al., 2007; Yuan et al., 2010). More specifically, the galaxies of the *red* and *cyan* clusters display starburst characteristics, such as prominent PAH emission and silicate dust absorption signals, in line with the emission signals of *LINER* and H_{II} galaxies. The clusters on the other end of the graph showcase AGN-luminous quasars properties: The *green* and *yellow* clusters display extinguished PAH emission and silicate dust absorption signals, in line with *Type-I Seyfert* luminous quasars. An intermediate phase of both starburst and AGN-dominated galaxies is identified in the *orange* cluster. The mean signal of the orange cluster also indicates the inclusion of many *Type-II Seyfert* galaxies: AGN-dominated galaxies that are observed with a steep viewing angle (edge-on), where the SMBH in their core is heavily shrouded by a dusty torus (hence

the presence of a moderate silicate dust absorption feature). This suggests a transition between the evolutionary phases of the power sources of the host galaxies, from the top-right to the bottom-left of our graph (red-cyan-orange-green-yellow clusters). This interpretation of our results is in agreement with Hurley et al. (2012).

Further examination on the nature of the galaxies in each cluster, can be made by investigating the nuclear separation of the host nuclei of each galaxy, shown in B.8, as well as the optical spectral type of each galaxy, as shown in B.9. The sample's nuclear separation distances in B.8 are presented in colors (for the available data), similar to Farrah et al. (2009) as: Cyan: > 12 kpc, Green: $6 - 12$ kpc, Yellow: $0.1 - 6$ kpc and Red: < 0.1 kpc (single nucleus). Noticeably, the galaxies displaying the highest nuclear separations (cyan and green) are concentrated on the top-right of our graph, matching the cyan and red colored clusters identified by the Shi and Malik (2000) spectral algorithm. Inversely, the galaxies with a single nucleus (red) are mostly concentrated in the middle and bottom-left of our graph, where the AGN-dominated clusters are identified by the algorithm. The low-intermediate nuclear separation galaxies (yellow) are spread throughout the graph.

The optical spectral types of the galaxies in our sample (where available) are presented in color in B.9, similar to Farrah et al. (2009). Specifically, cyan galaxies represent H_{II} , green galaxies are LINERs, while Seyfert-2 galaxies are shown in yellow and Seyfert-1/quasars are shown in red color. As expected, the starburst-dominated H_{II} and LINER galaxies are concentrated in the cyan and red clusters. Seyfert-2 galaxies are mostly present in the orange cluster and Seyfert-1/quasars are mostly seen in the yellow and green clusters, with some also present in the orange cluster. This is also another validation and verification of the detected clusters from our implementation of the Shi and Malik (2000) spectral algorithm.

Therefore, the clusters detected by the implementation of the Shi and Malik (2000) algorithm can be interpreted as:

- *Red* cluster = Starburst dominated ULIRGs, mostly LINERs, with high PAH emission and silicate dust absorption features.
- *Cyan* cluster = Starburst dominated ULIRGs, mostly H_{II} galaxies, with high-to-moderate PAH emission and silicate dust absorption features.
- *Orange* cluster = Both starburst and AGN dominated ULIRGs, with somewhat diminished PAH emission and a moderate silicate dust absorption feature. This is caused by the presence of mostly Type-II Seyfert galaxies, as well as some Type-I Seyfert/quasars, in this cluster.
- *Green and yellow* clusters = AGN dominated luminous quasars - Type-I Seyfert galaxies, with a single nucleus, showing completely extinguished PAH emission and silicate dust absorption features, as the AGN is the main power source.

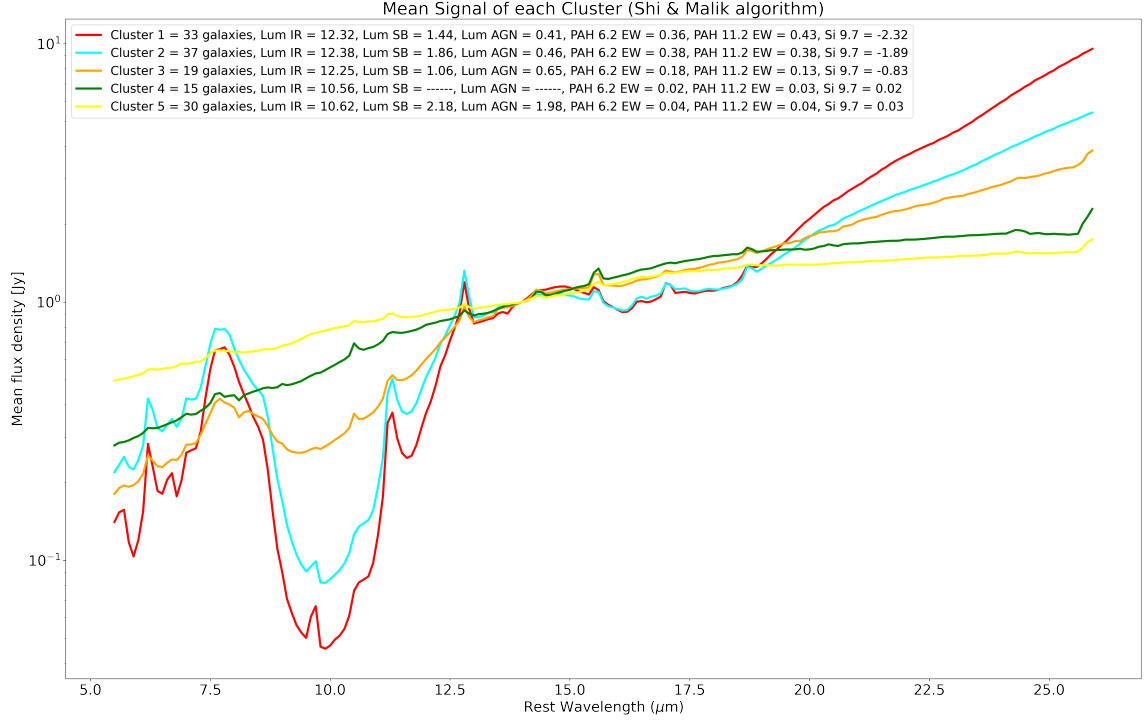


Figure 5: Mean mid-IR signals of each cluster detected via the Shi and Malik (2000) algorithm. Each signal represents the mean flux density calculated based on the galaxies of each cluster, normalized at $14\mu\text{m}$. The mean IR luminosity (Lum IR) in units $\log_{10}(L_{IR}/L_{\odot})$, the mean starburst luminosity (Lum SB) in units of $10^{12}L_{\odot}$ taken from Efstathiou et al. (2022), the mean AGN luminosity (Lum AGN) in units of $10^{12}L_{\odot}$ taken from Efstathiou et al. (2022), the mean PAH equivalent width values at $6.2\mu\text{m}$ (PAH 6.2 EW) and $11.2\mu\text{m}$ (PAH 11.2 EW), as well as the mean silicate absorption strength at $9.7\mu\text{m}$ (Si 9.7) of each cluster are shown in the legend on the top-left. Red and cyan-colored signals display mostly starburst-dominated ULIRG characteristics, the orange-colored signal is displays a mixture of starburst-dominated and AGN-dominated (mostly Seyfert-2) galaxies, and the green and yellow-colored signals represent AGN-dominated quasars (Seyfert-1) galaxies. The extinction of PAH emission and dust absorption features is apparent in the mean signals of AGN-dominated galaxies (green and yellow galaxies).

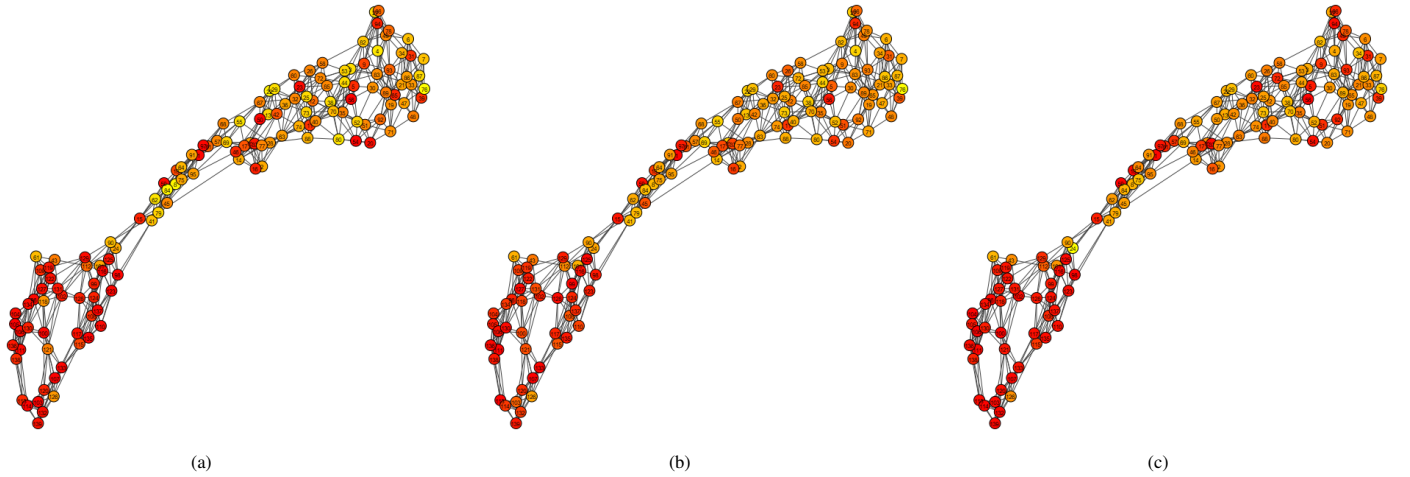


Figure 6: Colormaps of our graph based on (a) the $6.2\mu\text{m}$ PAH equivalent width emission, (b) the $11.2\mu\text{m}$ PAH equivalent width emission and (c) the Silicate dust absorption of galaxies. Yellow colors denote higher PAH equivalent widths and deeper silicate absorption, whereas red colors denote extinct values for PAH equivalent widths and silicate absorption. Orange nodes correspond to moderate values of PAH equivalent widths and silicate absorption.

In Figures 6a, 6b and 6c we present colormaps based on the calculated $6.2\mu\text{m}$, $11.2\mu\text{m}$ PAH equivalent widths and the $9.7\mu\text{m}$ silicate dust absorption feature of our galaxy samples. ULIRGs with high PAH equivalent width values and deep silicate absorption are colored yellow, whereas ULIRGs with extinct PAH and silicate features are colored red. ULIRGs showcasing intermediate (moderate) values of PAH emission and silicate absorption are colored orange. As expected, the colormaps showcase a trend of higher values of PAH emission and silicate dust absorption features for starburst galaxies on the top-right part of the graph and lower values for AGN-dominated luminous quasars towards the bottom-left of the graph. This result is in agreement with the theoretical model proposed by the merger scenario for ULIRGs: As these galaxies interact in the pre-merger stage, they display high PAH emission due to the increase in star-forming activity and the presence of more star-forming regions becomes more prominent (Figure 6a, Figure 6b). After the coalescence phase, the galaxies merge and their SMBHs become active. This results in the AGN IR emission becoming more dominant and the extinction of the PAH emission features.

Similarly, the silicate dust absorption feature in Figure 6c, correlated with the presence of a dust obscured AGN (buried AGN), becomes less distinguishable and almost extinct in the post-merger phase (bottom left of the graph). The galaxies in the intermediate phase (middle of the graph) still showcase a silicate dust absorption feature, which would suggest the presence of an AGN obscured by a dusty torus at this stage.

5.3.1. Comparison of detected communities with physical properties

An open question in galaxy classification is whether the communities detected using the galaxy spectra are directly correlated to their physical properties, particularly their PAH emission features as well as their silicate absorption/emission feature. Graph theory allows for this multi-variable comparison of galaxies' physical properties in a visual way, by drawing a colored graph, where the color of the node indicates its assigned community and at the same time assign nodes sizes analogous to one of the physical properties under investigation (i.e. PAH emission and Silicate absorption/emission features).

Figure 7a shows our graph with node colors indicating their corresponding community detected using the Shi and Malik (2000) spectral graph clustering algorithm and node sizes analogous to their PAH equivalent width emission feature at $6.2\mu\text{m}$. In Figure 7b we present the same graph, colored based on the Shi and Malik (2000) algorithm detected clusters and the node sizes corresponding to their silicate absorption feature. In both figures, nodes with larger sizes represent ULIRGs with high PAH equivalent width values and deeper silicate absorption features, respectively. Conversely, nodes with smaller sizes represent ULIRGs with extinct PAH equivalent width and silicate absorption features. The distinction of different values of these features between these communities is immediately apparent. The red and cyan-colored clusters on one end of the graph display higher

overall PAH emission and silicate absorption features, compared to the yellow and green-colored clusters at the other end of the graph. These features indicate that starburst activity is more evident in the red and cyan-colored clusters, whereas they become mostly extinct in the yellow and green-colored clusters, suggesting the presence of AGN activity in these galaxies.

By viewing figures 7a and 7b in conjunction with the fork diagrams in figures 8a and 8b we can gauge the success of the implementation of the Shi and Malik (2000) algorithm and our overall methodology in classifying galaxies based on the physical properties of their mid-IR emission. The clusters detected clearly correspond to different evolutionary stages of the merger scenario of ULIRGs. Therefore, our graph could be interpreted as a quasi-linear progression in the evolution of ULIRGs, from the starburst-dominated pre-merger stage (red and blue clusters) towards the AGN-dominated post-merger stage (green and yellow clusters).

5.4. Comparison with Related Works

5.4.1. The fork diagram

Following the *fork* diagnostic diagram introduced by Spoon et al. (2007), we can examine the clustering algorithm detected communities plotted on a 2-dimensional space, where the x -axis represents the PAH emission feature and the y -axis represents the silicate dust absorption feature. In Figures 8a and 8b we present the *fork* diagrams with the galaxies color-coded based on the clusters identified by the implementation of the Shi and Malik (2000) spectral graph clustering algorithm (Figure 3b). In these diagrams the galaxies are distributed on the y -axis based on the value of their silicate dust absorption feature and on the x -axis based on the value of their PAH equivalent width at $6.2\mu\text{m}$ (Figure 8a) and $11.2\mu\text{m}$ (Figure 8b). As expected, the starburst galaxies of the red and cyan-colored clusters (which correspond to LINERs and H_{II} type galaxies) mostly correlate to higher PAH emission and silicate absorption features, whereas the AGN-dominated luminous quasars of the yellow and green-colored clusters correlate to very low PAH emission and extinct silicate absorption features. The orange-colored cluster galaxies are spread throughout the diagram, corresponding to a mix of both starburst and AGN-dominated galaxies.

By comparing the distribution of galaxies within the nine regions (1A-3C) presented in Spoon et al. (2007), where numbers 1 – 3 correspond to three separate regions of increasing silicate absorption (in ascending order) and letters A-C correspond to three regions of increasing PAH emission (alphabetically), we observe that our classification scheme (through clustering analysis) suggests a distribution of the *five* classes of galaxies into the nine regions proposed by Spoon et al. (2007) in the following way:

- The *red* cluster: mainly in regions 3A-3B and 2A-2C.
- The *cyan* cluster: mainly in regions 3A-3B and 2B-2C.
- The *orange* cluster: in regions 3B, 2A-2C and 1A-1B.

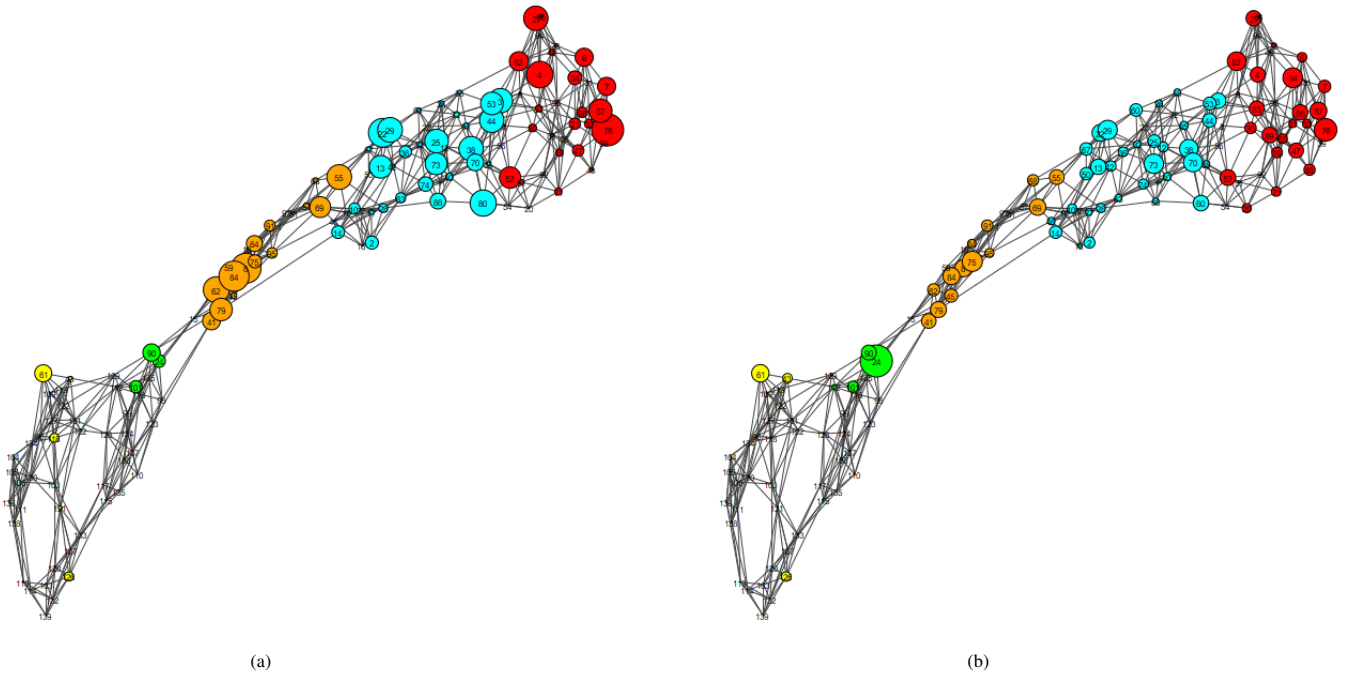
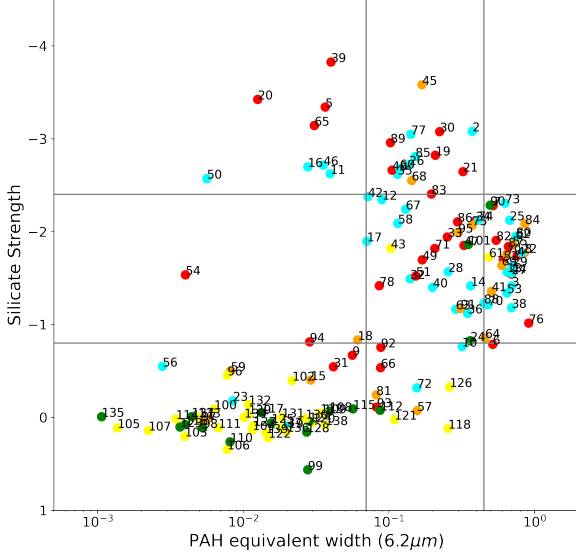


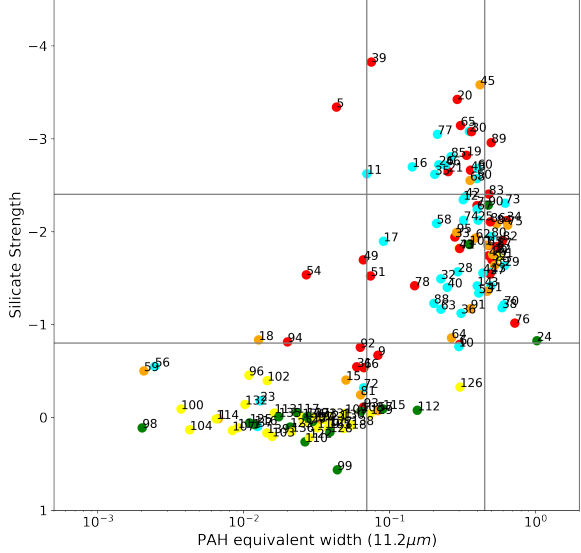
Figure 7: Communities detected using the spectral clustering algorithm of Shi and Malik (2000), in different colors. The node sizes represent (a) the PAH equivalent width emission feature and (b) the Silicate/emission feature. ULIRGs with high PAH emission equivalent widths and deeper silicate absorption features correspond to larger node sizes, whereas ULIRGs with extinct values for both features correspond to smaller node sizes. The transition from weak to strong PAH and Si features, between PG quasars (orange - cyan clusters) and starburst galaxies (green - yellow clusters), is clearly observable.

Spoon diagram - Farrah & PG quasar data - Shi & Malik 5 Clusters - for PAH 6.2 microns



(a)

Spoon diagram - Farrah & PG quasar data - Shi & Malik 5 Clusters - for PAH 11.2 microns



(b)

Figure 8: Fork diagrams, as introduced in Spoon et al. (2007), with galaxies color coded based on the clusters detected using the spectral clustering algorithm of Shi and Malik (2000). The galaxies are distributed based on their silicate dust absorption feature (y-axis) and their (a) 6.2 μm and (b) 11.2 μm PAH emission features (x-axis). The diagram is separated into the nine regions (1A-3C) proposed by Spoon et al. (2007). The yellow and green-colored communities showcase features correlated to AGN-dominated quasars, whereas the red and cyan-colored communities showcase features of starburst-dominated galaxies. The orange-colored community indicates a mix of both starburst & AGN-dominated galaxies.

- The *green* cluster: mainly in regions 2B-2C and 1A-1B.
- The *yellow* cluster: contained mainly within regions 1A-1B, with a few outliers also present in region 2B.

Overall, the performance of our clustering analysis, and the implementation of the spectral graph clustering algorithm of Shi and Malik (2000) in particular, is in agreement with the distinct physical properties of the different regions, as proposed by Spoon et al. (2007). Although there is an observed overlap of galaxy clusters within some of the regions, the containment of most of the galaxies of each cluster within specific regions is an important indicator of the good performance of the algorithm.

5.4.2. Archetypical galaxies of each cluster

By considering the observed features and physical properties of specific *archetypical* galaxies for each of the detected clusters, we can further examine the evolution of power sources between clusters. The selection of these archetypical galaxies is initially based on the calculated *local clustering coefficient* of individual galaxies (e.g. the probability that two neighbors of a vertex are connected), compared to the *global clustering coefficient* of our graph (which is based on the ratio of connected triplets over all triangles of nodes in the graph). The chosen archetypical galaxies of each cluster display a higher clustering coefficient compared to the rest of the graph, meaning that they are more highly connected compared to the rest of the graph, and thus they can be interpreted as indicative for each local cluster. Additionally, where available, we select well-known galaxies as archetypical galaxies, based on established literature, namely *Arp 220* (7) and *3C 273* (96) for the red and yellow clusters respectively.

Beginning from the red cluster, *Arp 220* (7) is a well known starburst galaxy, classified as a LINER type galaxy, displaying both high silicate absorption and high PAH emission features, as shown in Figures 8a and 8b. This indicates a high dust content around its power source, as well as high star-forming activity. *Arp 220* also shows low nuclear separation, between 0.1-6 kpc (Figure B.8).

Considering the cyan cluster, *IRAS 17068+4027* (74) is an H_{II} type starburst galaxy (Figure B.9), which displays high nuclear separation (Figure B.8) and moderately high silicate absorption and PAH emission features (Figures 8a and 8b). These properties are consistent with the features observed in the cyan cluster's mean signal, in Figure 5.

Regarding the orange cluster, it is a mixed cluster which presents moderate features of silicate absorption and PAH emission, thus we consider two archetypical galaxies: *IRAS 00275-2859* (15) and *IRAS 17179+5444* (75). The former is a Seyfert-I type galaxy which displays low silicate absorption and PAH emission features (Figures 8a and 8b). The latter is a Seyfert-II type galaxy, which also displays moderate silicate absorption but high PAH emission features. This combination goes some way to explaining the moderate features observed in the mean signal

of the cluster, as this cluster is mostly populated by Seyfert-II type galaxies, but also contains a mixture of starburst galaxies and quasars. Both galaxies also display a very low nuclear separation (single nucleus), as shown in Figure B.8.

The quasar *PG 0934+013* (116) could be considered as the archetypical galaxy for the green cluster, which (as expected) displays very low nuclear separation (single nucleus). This quasar displays almost no silicate absorption, as well as nearly extinct PAH emission features (Figures 8a and 8b).

3C 273 (96) is a well known quasar that could be considered as the archetypical galaxy of the yellow cluster, displaying all of the expected features for a quasar. Specifically, *3C 273* shows very low nuclear separation (Figure B.8), as well as very low silicate absorption and highly extinct PAH emission features. This is in-line with the observed mean signal of the yellow cluster. As mentioned above, considering the fork diagrams of Figures 8a and 8b, most of the yellow cluster quasars show no silicate absorption (or even silicate emission) as well as very low (extinct) PAH emission features. These features may be the main cause for the distinction between the green and yellow clusters by our clustering algorithms.

5.4.3. Graph Theoretic Evolutionary Path

The partitioning of the similarity graph into clusters combined with the characterization of the SED communities in relation to the physical properties of the galaxies, also reveals some relation between the communities themselves. Through the partitioning obtained by all graph clustering algorithms tested, we can observe that - besides the agreement on the number of clusters detected - in all algorithms' outcomes, each one of the identified clusters has two other neighbouring clusters in the graph, forming all together a *path* connecting the neighbouring clusters. Moreover, PAH emission and silicate absorption features gradually increase/decrease between neighbouring clusters. Combining these results seems to suggest a possible quasi-linear evolutionary path for the power sources of ULIRGs.

Thus, the results of our graph theoretical methodology indicate a transitional evolution between different types of galaxies, with the pre-merger evolutionary phase being populated by mostly dust-obscured starburst-dominated galaxies (mainly LINERs and H_{II} galaxies), while the coalescence phase being populated by a combination of starburst and obscured AGN-dominated galaxies (mostly Type-II and some Type-I Seyferts), and finally the post-merger phase being populated by mostly unobscured AGN-dominated galaxies and luminous quasars. While previous works (e.g. Farrah et al. (2009)) also suggest the possibility of the merger scenario following two distinct evolutionary paths, our results showcase a single evolutionary scenario for mergers. However, this result could be subject to further investigation.

6. Conclusions

We have presented how graph theoretical and clustering analysis tools can be utilized for the classification of galaxies based on their mid-IR spectra, in order to extract meaningful information on the underlying mechanisms. We have showcased the successful implementation of KPCA on mid-IR spectra of ULIRGs for the construction of a similarity graph, as well as utilizing clustering algorithms in order to extract different communities, corresponding to separate evolutionary stages. Furthermore, the examination of the physical properties of the identified communities led to a physical interpretation supporting the evolutionary merger scenario for ULIRGs.

More specifically, we have presented how our graph theoretical methodology results in an evolutionary paradigm for ULIRGs supporting the merger scenario, by showcasing a quasi-linear transition of the dominant power sources of ULIRGs, from the dust-obscured starburst-dominated galaxies of the pre-merger phase towards the unobscured AGN-dominated luminous quasars of the post-merger phase.

Additionally, we have tested and compared the performance of multiple different clustering algorithms on astrophysical data, based on graph theoretical metrics as well as in comparison to the existing theoretical framework for galaxy evolution.

Future works utilizing higher-resolution mid-infrared ULIRG spectra (obtained by future missions such as the James Webb Space Telescope), as well as extended catalogues of ULIRGs, can result in defining a much more concrete evolutionary paradigm for the merger scenario of ULIRGs. Furthermore, future examination of additional graph theoretical approaches in studying galaxy evolution, as well as potential comparisons of the mid-infrared spectra of ULIRGs across different redshift ranges, could offer important insights on the nature and physical mechanisms of galaxy evolution throughout the history of the Universe.

Acknowledgements

The authors acknowledge support from the research project *EXCELLENCE/1216/0207* - "Graph Theoretical Tools in Sciences" (*GRATOS*) funded by the Research & Innovation Foundation (RIF) in Cyprus.

Data Availability Statement

The observational data used for the purposes of this article are available in the Combined Atlas of Sources with Spitzer IRS Spectra (CASSIS) website. Some of the results of the graph theoretical analysis of the data, generated as part of the aforementioned research project *EXCELLENCE/1216/0207* (*GRATOS*) used in this article are available on the website of the project at Aristarchus Research Center website.

References

- Antonucci, R., 1993. Unified models for active galactic nuclei and quasars. *ARAA* 31, 473–521. URL: <https://doi.org/10.1146/annurev.aa.31.090193.002353>, doi:10.1146/annurev.aa.31.090193.002353, arXiv:<https://doi.org/10.1146/annurev.aa.31.090193.002353>.
- Barabási, A.L., Pósfai, M., 2016. Network science. Cambridge University Press, Cambridge. URL: <http://barabasi.com/networksciencebook/>.
- Barger, A.J., Cowie, L.L., Sanders, D.B., Fulton, E., Taniguchi, Y., Sato, Y., Kawara, K., Okuda, H., 1998. Submillimetre-wavelength detection of dusty star-forming galaxies at high redshift. *Nature* 394, 248–251. URL: <http://dx.doi.org/10.1038/28338>, doi:10.1038/28338.
- Blondel, V.D., Gajardo, A., Heymans, M., Senellart, P., Van Dooren, P., 2004. A measure of similarity between graph vertices: Applications to synonym extraction and web searching. *SIAM Review* 46, 647–666. URL: <https://doi.org/10.1137/S0036144502415960>, doi:10.1137/S0036144502415960, arXiv:<https://doi.org/10.1137/S0036144502415960>.
- Blondel, V.D., Guillaume, J.L., Lambiotte, R., Lefebvre, E., 2008a. Fast unfolding of communities in large networks. *Journal of Statistical Mechanics: Theory and Experiment* 2008.
- Blondel, V.D., Guillaume, J.L., Lambiotte, R., Lefebvre, E., 2008b. Fast unfolding of communities in large networks. *Journal of Statistical Mechanics: Theory and Experiment* 2008.
- Brandes, U., Delling, D., Gaertler, M., Gorke, R., Hoefer, M., Nikoloski, Z., Wagner, D., 2008. On modularity clustering. *IEEE Transactions on Knowledge and Data Engineering* 20, 172–188. doi:10.1109/TKDE.2007.190689.
- Bruzual, G., Charlot, S., 1993. Spectral Evolution of Stellar Populations Using Isochrone Synthesis. *ApJ* 405, 538. doi:10.1086/172385.
- Bruzual, G., Charlot, S., 2003. Stellar population synthesis at the resolution of 2003. *MNRAS* 344, 1000–1028. doi:10.1046/j.1365-8711.2003.06897.x, arXiv:[astro-ph/0309134](https://arxiv.org/abs/astro-ph/0309134).
- Bullmore, E.T., Sporns, O., 2009. Complex brain networks: graph theoretical analysis of structural and functional systems. *Nature Reviews Neuroscience* 10, 186–198.
- Casey, C.M., Narayanan, D., Cooray, A., 2014. Dusty star-forming galaxies at high redshift. *Physics Reports* 541, 45–161. URL: <http://dx.doi.org/10.1016/j.physrep.2014.02.009>, doi:10.1016/j.physrep.2014.02.009.
- Coutinho, B.C., Hong, S., Albrecht, K., Dey, A., Barabási, A.L., Torrey, P., Vogelsberger, M., Hernquist, L., 2016. The network behind the cosmic web. <https://arxiv.org/abs/1604.03236>.
- Desai, V., Armus, L., Spoon, H.W.W., Charmandaris, V., Bernard-Salas, J., Brandl, B.R., Farrah, D., Soifer, B.T., Teplitz, H.I., Ogle, P.M., Devost, D., Higdon, S.J.U., Marshall, J.A., Houck, J.R., 2007. PAH emission from ultraluminous infrared galaxies*. *The Astrophysical Journal* 669, 810. URL: <https://dx.doi.org/10.1086/522104>, doi:10.1086/522104.
- Efstathiou, A., Christopher, N., Verma, A., Siebenmorgen, R., 2013. Active galactic nucleus torus models and the puzzling infrared spectrum of IRAS F10214+4724. *MNRAS* 436, 1873–1882. URL: <https://doi.org/10.1093/mnras/stt1695>, doi:10.1093/mnras/stt1695, arXiv:<https://academic.oup.com/mnras/article-pdf/436/2/1873/3956059/stt1695.pdf>.
- Efstathiou, A., Farrah, D., et al., 2022. A new look at local ultraluminous infrared galaxies: The atlas and radiative transfer models of their complex physics. *MNRAS* submitted. URL: <http://dx.doi.org/10.1093/mnras/slaa206>, doi:10.1093/mnras/slaa206.
- Efstathiou, A., Malek, K., Burgarella, D., Hurley, P., Oliver, S., Buat, V., Shirley, R., Duivenvoorden, S., Lesta, V.P., Farrah, D., et al., 2021. A hyperluminous obscured quasar at a redshift of $z \approx 4.3$. *MNRAS* 503, L11. URL: <http://dx.doi.org/10.1093/mnras/slaa206>, doi:10.1093/mnras/slaa206.
- Efstathiou, A., Pearson, C., Farrah, D., Rigopoulou, D., Graciá-Carpio, J., Verma, A., Spoon, H.W.W., Afonso, J., Bernard-Salas, J., Clements, D.L., Cooray, A., Cormier, D., Etxaluze, M., Fischer, J., González-Alfonso, E., Hurley, P., Lebouteiller, V., Oliver, S.J., Rowan-Robinson, M., Sturm, E., 2014. Herschel observations and a model for IRAS 08572+3915: a candidate for the most luminous infrared galaxy in the local ($z \lesssim 0.2$) Universe. *MNRAS* 437, L16–L20. URL: <https://doi.org/10.1093/mnras/s1t131>, doi:10.1093/mnras/s1t131,

- arXiv:<https://academic.oup.com/mnras/article-pdf/437/1/L16/6216995/slt131.pdf>.
- Efstathiou, A., Rowan-Robinson, M., 1995. Dusty discs in active galactic nuclei. *MNRAS* 273, 649–661. URL: <https://doi.org/10.1093/mnras/273.3.649>, doi:10.1093/mnras/273.3.649, arXiv:<https://academic.oup.com/mnras/article-pdf/273/3/649/18539698/mnras273-0649.pdf>.
- Efstathiou, A., Rowan-Robinson, M., 2003. Cirrus models for local and high- z SCUBA galaxies. *MNRAS* 343, 322–330. URL: <https://doi.org/10.1046/j.1365-8711.2003.06679.x>, doi:10.1046/j.1365-8711.2003.06679.x, arXiv:<https://academic.oup.com/mnras/article-pdf/343/1/322/3457165/343-1-322.pdf>.
- Efstathiou, A., Rowan-Robinson, M., Siebenmorgen, R., 2000. Massive star formation in galaxies: radiative transfer models of the UV to millimetre emission of starburst galaxies. *MNRAS* 313, 734–744. doi:10.1046/j.1365-8711.2000.03269.x, arXiv:[astro-ph/9912252](https://arxiv.org/abs/astro-ph/9912252).
- Efstathiou, A., Siebenmorgen, R., 2009. Starburst and cirrus models for submillimetre galaxies. *A&A* 502, 541–548. URL: <http://dx.doi.org/10.1051/0004-6361/200811205>, doi:10.1051/0004-6361/200811205.
- Farrah, D., Afonso, J., Efstathiou, A., Rowan-Robinson, M., Fox, M., Clements, D., 2003. Starburst and agn activity in ultraluminous infrared galaxies. *MNRAS* 343, 585–607. URL: <http://dx.doi.org/10.1046/j.1365-8711.2003.06696.x>, doi:10.1046/j.1365-8711.2003.06696.x.
- Farrah, D., Connolly, B., Connolly, N., Spoon, H.W.W., Oliver, S., Prosper, H.B., Armus, L., Houck, J.R., Liddle, A.R., Desai, V., 2009. AN EVOLUTIONARY PARADIGM FOR DUSTY ACTIVE GALAXIES AT LOW REDSHIFT. *ApJ* 700, 395–416. URL: <https://doi.org/10.1088/0004-637x/700/1/395>, doi:10.1088/0004-637x/700/1/395.
- Farrah, D., Lebouteiller, V., Spoon, H.W.W., Bernard-Salas, J., Pearson, C., Rigopoulou, D., Smith, H.A., González-Alfonso, E., Clements, D.L., Efstathiou, A., Cormier, D., Afonso, J., Petty, S.M., Harris, K., Hurley, P., Borys, C., Verma, A., Cooray, A., Salvatelli, V., 2013. FAR-INFRARED FINE-STRUCTURE LINE DIAGNOSTICS OF ULTRALUMINOUS INFRARED GALAXIES. *ApJ* 776, 38. URL: <https://doi.org/10.1088/0004-637x/776/1/38>, doi:10.1088/0004-637x/776/1/38.
- Farrah, D., Rowan-Robinson, M., Oliver, S., Serjeant, S., Borne, K., Lawrence, A., Lucas, R.A., Bushouse, H., Colina, L., 2001. Hst/wfpc2 imaging of the qdot ultraluminous infrared galaxy sample. *MNRAS* 326, 1333–1352. URL: <https://doi.org/10.1111/j.1365-2966.2001.04721.x>.
- Fortunato, S., 2010. Community detection in graphs. *Physics Reports* 486, 75–174. doi:10.1016/j.physrep.2009.11.002. <https://www.scopus.com/inward/record.uri?eid=2-s2.0-74049087026&doi=10.1016%2Fj.physrep.2009.11.002&partnerID=40&md5=3699306c53689109b2a0694078ff6197>.
- Fruchterman, T.M.J., Reingold, E.M., 1991. Graph drawing by force-directed placement. *Software: Practice and Experience* 21.
- Fu, H., Yan, L., Scoville, N.Z., Capak, P., Aussel, H., et al., 2010. Decomposing star formation and active galactic nucleus with spitzer mid-infrared spectra: Luminosity functions and co-evolution. *ApJ* 722, 653–667. URL: <https://iopscience.iop.org/article/10.1088/0004-637x/722/1/653>, doi:10.1088/0004-637x/722/1/653.
- Gao, F., Wang, L., Efstathiou, A., Małek, K., Best, P.N., Bonato, M., Farrah, D., Kondapally, R., McChesney, I., Röttgering, H.J.A., 2021. The nature of hyperluminous infrared galaxies. *A&A* 654, A117. doi:10.1051/0004-6361/202141358, arXiv:2107.08703.
- Genzel, R., Lutz, D., Sturm, E., Egami, E., Kunze, D., Moorwood, A.F.M., Rigopoulou, D., Spoon, H.W.W., Sternberg, A., Tacconi-Garman, L.E., et al., 1998. What powers ultraluminous iras galaxies? *ApJ* 498, 579. URL: <http://dx.doi.org/10.1086/305576>, doi:10.1086/305576.
- Girvan, M., Newman, M.E.J., 2002. Community structure in social and biological networks. *Proceedings of the National Academy of Sciences* 99, 7821–7826. URL: <https://www.pnas.org/content/99/12/7821>, doi:10.1073/pnas.122653799.
- Granato, G.L., Danese, L., 1994. Thick tori around active galactic nuclei: a comparison of model predictions with observations of the infrared continuum and silicate features. *MNRAS* 268, 235–252. URL: <https://doi.org/10.1093/mnras/268.1.235>, doi:10.1093/mnras/268.1.235, arXiv:<https://academic.oup.com/mnras/article-pdf/268/1/235/3196976/mnras268-0235.pdf>.
- Harris, K., Farrah, D., Schulz, B., Hatziminaoglou, E., Viero, M., Anderson, N., Béthermin, M., Chapman, S., Clements, D.L., Cooray, A., Efstathiou, A., Feltre, A., Hurley, P., Ibar, E., Lacy, M., Oliver, S., Page, M.J., Pérez-Fournon, I., Petty, S.M., Pitchford, L.K., Rigopoulou, D., Scott, D., Symeonidis, M., Vieira, J., Wang, L., 2016. Star formation rates in luminous quasars at $2 < z < 3$. *MNRAS* 457, 4179–4194. doi:10.1093/mnras/stw286, arXiv:1602.02755.
- Hong, S., Coutinho, B.C., Dey, A., Barabási, A.L., Vogelsberger, M., Hernquist, L., Gebhardt, K., 2016. Discriminating topology in galaxy distributions using network analysis. *MNRAS* 459, 2690–2700. URL: <http://dx.doi.org/10.1093/mnras/stw803>, doi:10.1093/mnras/stw803.
- Hong, S., Dey, A., 2015. Network analysis of cosmic structures : Network centrality and topological environment. *Monthly Notices of the Royal Astronomical Society* 450(2), 1999–2015.
- Houck, J.R., Roellig, T.L., van Cleve, J., Forrest, W.J., Herter, T., Lawrence, C.R., Matthews, K., Reitsema, H.J., Soifer, B.T., Watson, D.M., et al., 2004. The infrared spectrograph (irs) on the spitzer space telescope. *ApJS* 154, 18. URL: <http://dx.doi.org/10.1086/423134>, doi:10.1086/423134.
- Hughes, D.H., Serjeant, S., Dunlop, J., Rowan-Robinson, M., Blain, A., Mann, R.G., Ivison, R., Peacock, J., Efstathiou, A., Gear, W., et al., 1998. High-redshift star formation in the hubble deep field revealed by a submillimetre-wavelength survey. *Nature* 394, 241. URL: <http://dx.doi.org/10.1038/28328>, doi:10.1038/28328.
- Hurley, P.D., Oliver, S., Farrah, D., Wang, L., Efstathiou, A., 2012. Principal component analysis and radiative transfer modelling of Spitzer Infrared Spectrograph spectra of ultraluminous infrared galaxies. *MNRAS* 424, 2069–2078. URL: <https://doi.org/10.1111/j.1365-2966.2012.21352.x>, doi:10.1111/j.1365-2966.2012.21352.x, arXiv:<https://academic.oup.com/mnras/article-pdf/424/3/2069/2996469/424-3-2069.pdf>.
- Imanishi, I., Dudley, C.C., Maiolino, R., Maloney, P.R., Nakagawa, T., Risaliti, G., 2007. A spitzer irs low resolution spectroscopic search for buried agns in nearby ultraluminous infrared galaxies: a constraint on geometry between energy sources and dust. *ApJS* 171, 29.
- Ioannides, A.A., Kourouyannis, C., Karitvelis, C., Liu, L., Michos, I., Papadopoulos, M., Papaefthymiou, E., Pavlou, O., Papadopoulou, Lesta, V., Efstathiou, A., 2022. A unified framework for analyzing complex systems: Juxtaposing the (kernel) pca method and graph theory. *Frontiers in Applied Mathematics and Statistics* 8. URL: <https://www.frontiersin.org/articles/10.3389/fams.2022.947053>, doi:10.3389/fams.2022.947053.
- Kewley, L.J., Groves, B., Kauffmann, G., Heckman, T., 2006. The host galaxies and classification of active galactic nuclei. *MNRAS* 372, 961–976. URL: <https://doi.org/10.1111/j.1365-2966.2006.10859.x>, doi:10.1111/j.1365-2966.2006.10859.x.
- Kirkpatrick, A., Pope, A., Sajina, A., Roebuck, E., Yan, L., Armus, L., Diaz-Santos, T., Stierwalt, S., 2015. The role of star formation and an agn in dust heating of $z=0.3-2.8$ galaxies. i. evolution with redshift and luminosity. *ApJ* 814, 9. URL: <http://dx.doi.org/10.1088/0004-637x/814/1/9>, doi:10.1088/0004-637x/814/1/9.
- Kirkpatrick, A., Urry, C.M., Brewster, J., Cooke, K.C., Estrada, M., Glikman, E., Hamblin, K., Ananna, T.T., Carlile, C., Coleman, B., et al., 2020. The accretion history of agn: A newly defined population of cold quasars. *ApJ* 900, 5. URL: <http://dx.doi.org/10.3847/1538-4357/aba358>, doi:10.3847/1538-4357/aba358.
- Kobourov, S.G., 2012. Spring Embedders and Force Directed Graph Drawing Algorithms. arXiv e-prints, arXiv:1201.3011arXiv:1201.3011.
- Lebouteiller, V., Barry, D.J., Goes, C., Sloan, G.C., Spoon, H.W.W., Weedman, D.W., Bernard-Salas, J., Houck, J.R., 2015. Cassis: The cornell atlas of spitzer/infrared spectrograph sources. ii. high-resolution observations. *ApJS* 218, 21. URL: <http://dx.doi.org/10.1088/0067-0049/218/2/21>, doi:10.1088/0067-0049/218/2/21.
- Lebouteiller, V., Barry, D.J., Spoon, H.W.W., Bernard-Salas, J., Sloan, G.C., Houck, J.R., Weedman, D.W., 2011. CASSIS: THE CORNELL ATLAS OF SPITZER /INFRARED SPECTROGRAPH SOURCES. *ApJS* 196, 8. URL: <https://doi.org/10.1088/0067-0049/196/1/8>, doi:10.1088/0067-0049/196/1/8.
- Lian, J., Naik, K., Agnew, G.B., 2007. A framework for evaluating the performance of cluster algorithms for hierarchical networks. *IEEE/ACM Transactions on Networking* 15, 1478–1489.
- von Luxburg, U., 2007. A tutorial on spectral clustering. arXiv:0711.0189.

- MacQueen, J., et al., 1967. Some methods for classification and analysis of multivariate observations, in: Proceedings of the fifth Berkeley symposium on mathematical statistics and probability, Oakland, CA, USA. pp. 281–297.
- Marshall, J., Herter, T., Armus, L., Charmandaris, V., Spoon, H., Bernard-Salas, J., Houck, J., 2007. Decomposing dusty galaxies. i. multicomponent spectral energy distribution fitting. *ApJ* 670, 129.
- Murata, K.L., Yamada, R., Oyabu, S., Kaneda, H., Ishihara, D., Yamagishi, M., Kokusho, T., Takeuchi, T.T., 2016. A relationship of polycyclic aromatic hydrocarbon features with galaxy merger in star-forming galaxies at $z < 0.2$. *Monthly Notices of the Royal Astronomical Society* 000, 1–14.
- Nardini, E.e.a., 2008. Spectral decomposition of starbursts and active galactic nuclei in 5–8 μm Spitzer-IRS spectra of local ultraluminous infrared galaxies. *MNRAS* 385, 130–134. URL: <https://doi.org/10.1111/j.1745-3933.2008.00450.x>, doi:10.1111/j.1745-3933.2008.00450.x.
- Neugebauer, G., Habing, H., van Duinen, R., Aumann, H., Baud, B., et al. C.B., 1984. The infrared astronomical satellite (iras) mission. *ApJ* 278, L1–L6.
- Newman, M., 2006. Finding community structure in networks using the eigenvectors of matrices. *Physical review. E, Statistical, nonlinear, and soft matter physics* 74, 036104. doi:10.1103/physreve.74.036104.
- Newman, M.E.J., 2004. Fast algorithm for detecting community structure in networks. *Phys. Rev. E* 69, 066133.
- Newman, M.E.J., Girvan, M., 2004. Finding and evaluating community structure in networks. *Phys. Rev. E* 69, 026113.
- Ng, A.Y., Jordan, M.I., Weiss, Y., 2001. On spectral clustering: Analysis and an algorithm. *ADVANCES IN NEURAL INFORMATION PROCESSING SYSTEMS*, 849–856.
- Papaefthymiou, E.S., Michos, I., Pavlou, O., Papadopoulou Lesta, V., Efstathiou, A., 2022. Classification of local ultraluminous infrared galaxies and quasars with kernel principal component analysis. *Monthly Notices of the Royal Astronomical Society* 517, 4162–4174. URL: <https://doi.org/10.1093/mnras/stac2917>, doi:10.1093/mnras/stac2917, arXiv:<https://academic.oup.com/mnras/article-pdf/517/3/4162/47170584/stac2917.pdf>.
- Peeters, E., Hony, S., Van Kerckhoven, C., Tielens, A. G. G. M., Allamandola, L. J., Hudgins, D. M., Bauschlicher, C. W., 2002. The rich 6 to 9 μm spectrum of interstellar pachs. *A&A* 390, 1089–1113. URL: <https://doi.org/10.1051/0004-6361:20020773>, doi:10.1051/0004-6361:20020773.
- Pérez-Torres, M., Mattila, S., Alonso-Herrero, A., Aalto, S., Efstathiou, A., 2021. Star formation and nuclear activity in luminous infrared galaxies: an infrared through radio review. *A&A Rev.* 29, 2. doi:10.1007/s00159-020-00128-x, arXiv:2010.05072.
- Pier, E., Krolik, J., 1992. Infrared spectra of obscuring dust tori around active galactic nuclei. i - calculational method and basic trends. *ApJ* 401, 99–109.
- Pitchford, L.K., Hatziminaoglou, E., Feltre, A., Farrah, D., Clarke, C., Harris, K.A., Hurley, P., Oliver, S., Page, M., Wang, L., 2016. Extreme star formation events in quasar hosts over $0.5 < z < 4$. *MNRAS* 462, 4067–4077. doi:10.1093/mnras/stw1840, arXiv:1607.06459.
- Pons, P., Latapy, M., 2006. Computing communities in large networks using random walks. *J. Graph Algorithms Appl*, 191–218.
- Radicchi, F., Castellano, C., Cecconi, F., Loreto, V., Parisi, D., 2004. Defining and identifying communities in networks. *Proceedings of the National Academy of Sciences* 101, 2658–2663. doi:10.1073/pnas.0400054101. <https://www.pnas.org/content/101/9/2658>.
- Rigopoulou, D., Spoon, H.W.W., Genzel, R., Lutz, D., Moorwood, A.F.M., Tran, Q.D., 1999. A large mid-infrared spectroscopic and near-infrared imaging survey of ultraluminous infrared galaxies: Their nature and evolution. *AJ* 118, 2625. URL: <https://doi.org/10.1086/301146>, doi:10.1086/301146.
- Roche, P.F., Aitken, D.K., Smith, C.H., 1991. The structure of the narrow emission bands near 10 μm . *MNRAS* 252, 282–287. URL: <https://doi.org/10.1093/mnras/252.2.282>, doi:10.1093/mnras/252.2.282, arXiv:<https://academic.oup.com/mnras/article-pdf/252/2/282/3932688/mnras252-0282.pdf>.
- Rodighiero, G., Vaccari, M., Franceschini, A., Tresse, L., Le Fevre, O., Le Brun, V., Mancini, C., Matute, I., Cimatti, A., Marchetti, L., Ilbert, O., Arnouts, S., Bolzonella, M., Zucca, E., Bardelli, S., Lonsdale, C. J., Shupe, D., Surace, J., Rowan-Robinson, M., Garilli, B., Zamorani, G., Pozzetti, L., Bondi, M., de la Torre, S., Vergani, D., Santini, P., Grazian, A., Fontana, A., 2010. Mid- and far-infrared luminosity functions and galaxy evolution from multiwavelength spitzer observations up to $z = 2.5$. *Astronomy & Astrophysics* 515.
- Rowan-Robinson, M., Efstathiou, A., 1993. Multigrain dust cloud models of starburst and Seyfert galaxies. *MNRAS* 263, 675–680. URL: <https://doi.org/10.1093/mnras/263.3.675>, doi:10.1093/mnras/263.3.675, arXiv:<https://academic.oup.com/mnras/article-pdf/263/3/675/4039461/mnras263-0675.pdf>.
- Rowan-Robinson, M., Efstathiou, A., Lawrence, A., Oliver, S., Taylor, A., Broadhurst, T.J., McMahon, R.G., Benn, C.R., Condon, J.J., Lonsdale, C.J., Hacking, P., Conrow, T., Saunders, W.S., Clements, D.L., Ellis, R.S., Robson, I., 1993. The ultraviolet-to-radio continuum of the ultraluminous galaxy IRAS F10214+4724. *MNRAS* 261, 513–521. doi:10.1093/mnras/261.3.513.
- Rowan-Robinson, M., Wang, Lingyu, Farrah, Duncan, Rigopoulou, Dimitra, Gruppioni, Carlotta, Vaccari, Mattia, Marchetti, Lucia, Clements, David L., Pearson, William J., 2018. Extreme submillimetre starburst galaxies. *A&A* 619, 169. URL: <https://doi.org/10.1051/0004-6361/201832671>, doi:10.1051/0004-6361/201832671.
- Sabiu, C.G., Hoyle, B., Kim, J., Li, X.D., 2019. Graph database solution for higher-order spatial statistics in the era of big data. *The Astrophysical Journal Supplement Series* 242(2).
- Sajina, A., Yan, L., Fadda, D., Dasyra, K., Huynh, M., 2012. Spitzer and herchel-based spectral energy distributions of 24 μm bright $z = 0.3$ – 3.0 starbursts and obscured quasars. *ApJ* 757, 13. URL: <https://iopscience.iop.org/article/10.1088/0004-637X/757/1/13>, doi:10.1088/0004-637X/757/1/13.
- Sanders, D., Soifer, B., Elias, J., Madore, B., Matthews, K., Neugebauer, G., Scoville, N., 1988. Ultraluminous infrared galaxies and the origin of quasars. *ApJ* 325, 74–91.
- Sanders, D.B., Mirabel, I.F., 1996. Luminous infrared galaxies. *ARAAS* 34, 749–792. URL: <https://doi.org/10.1146/annurev.astro.34.1.749>, doi:10.1146/annurev.astro.34.1.749, arXiv:<https://doi.org/10.1146/annurev.astro.34.1.749>.
- Schreiber, C., Pannella, M., Elbaz, D., Béthermin, M., Inami, H., Dickinson, M., Magnelli, B., Wang, T., Aussel, H., Daddi, E., Juneau, S., Shu, X., Sargent, M.T., Buat, V., Faber, S.M., Ferguson, H.C., Giavalisco, M., Koekemoer, A.M., Magdis, G., Morrison, G.E., Papovich, C., Santini, P., Scott, D., 2015. The herchel view of the dominant mode of galaxy growth from $z = 4$ to the present day. *Astronomy & Astrophysics* 575.
- Shi, J., Malik, J., 2000. Normalized cuts and image segmentation. *IEEE Transactions on Pattern Analysis and Machine Intelligence* 22, 888–905. doi:10.1109/34.868688.
- Shipley, H.V., Papovich, C., Rieke, G.H., Brown, M.J.I., Moustakas, J., 2016. A new star formation rate calibration from polycyclic aromatic hydrocarbon emission features and application to high-redshift galaxies. *The Astrophysical Journal* 818, 60–80.
- Shirley, R., Duncan, K., Campos Varillas, M.C., Hurley, P.D., Malek, K., Roehly, Y., Smith, M.W.L., Aussel, H., Bakx, T., Buat, V., Burgarella, D., Christopher, N., Duivenvoorden, S., Eales, S., Efstathiou, A., González Solares, E.A., Griffin, M., Jarvis, M., Faro, B.L., Marchetti, L., McCheyne, I., Papadopoulos, A., Penner, K., Pons, E., Prescott, M., Rigby, E., Rottgering, H., Saxena, A., Scudder, J., Vaccari, M., Wang, L., Oliver, S.J., 2021. HELP: the herchel extragalactic legacy project. *MNRAS* 507, 129–155. doi:10.1093/mnras/stab1526, arXiv:2105.05659.
- Shirley, R., Roehly, Y., Hurley, P.D., Buat, V., Campos Varillas, M.d.C., Duivenvoorden, S., Duncan, K.J., Efstathiou, A., Farrah, D., González Solares, E., Malek, K., Marchetti, L., McCheyne, I., Papadopoulos, A., Pons, E., Scipioni, R., Vaccari, M., Oliver, S., 2019. HELP: a catalogue of 170 million objects, selected at 0.36–4.5 μm , from 1270 deg² of prime extragalactic fields. *MNRAS* 490, 634–656. doi:10.1093/mnras/stz2509, arXiv:1909.04003.
- Siebenmorgen, R., Krugel, E., 2007. Dust in starburst nuclei and ulirgs. *A&A* 461, 445–453. URL: <https://www.aanda.org/articles/aa/abs/2007/02/aa5700-06/aa5700-06.html>, doi:10.1051/0004-6361:20065700.
- Silva, L., Granato, G.L., Bressan, A., Danese, L., 1998. Modeling the effects of dust on galactic spectral energy distributions from the ultraviolet to the millimeter band. *ApJ* 509, 103–117. URL: <http://dx.doi.org/10.1086/306476>, doi:10.1086/306476.
- Soifer, B., Sanders, D., Madore, B., Neugebauer, G., Danielson, G., Elias, J., Lonsdale, J., Carol, J., Rice, W., 1987. The iras bright galaxy sample. ii. the sample and luminosity function. *ApJ* 320, 238.
- Spoon, H.W.W., Armus, L., Cami, J., Tielens, A.G.G.M., Chiar, J.E., Peeters,

E., Keane, J.V., Charmandaris, V., Appleton, P.N., Teplitz, H.I., 2004. Fire and ice: Spitzer infrared spectrograph (irs) mid-infrared spectroscopy of iras f00183–7111. *ApJ* 154, 184. URL: <https://iopscience.iop.org/article/10.1086/422813>, doi:10.1086/422813.

Spoon, H.W.W., Marshall, J.A., Houck, J.R., Elitzur, M., Hao, L., Armus, L., Brandl, B.R., Charmandaris, V., 2007. Mid-infrared galaxy classification based on silicate obscuration and PAH equivalent width. *ApJ* 654, L49–L52. URL: <https://doi.org/10.1086/511268>, doi:10.1086/511268.

Sturm, E., Lutz, D., Tran, D., Feuchtgruber, H., Genzel, R., Kunze, D., Moorwood, A.F.M., Thornley, M.D., 2000. ISO-SWS spectra of galaxies: Continuum and features. *A&A* 358, 481–493.

Symeonidis, M., Giblin, B.M., Page, M.J., Pearson, C., Bendo, G., Seymour, N., Oliver, S.J., 2016. AGN are cooler than you think: the intrinsic far-IR emission from QSOs. *MNRAS* 459, 257–276. URL: <https://doi.org/10.1093/mnras/stw667>, doi:10.1093/mnras/stw667, arXiv:<https://academic.oup.com/mnras/article-pdf/459/1/257/13773393/stw667.pdf>.

Traag, V., Waltman, L., van Eck, N.J., 2019. From louvain to leiden: guaranteeing well-connected communities. *Scientific Reports* 9, 5233. doi:10.1038/s41598-019-41695-z.

Ueda, H., Takeuchi, T. T., Itoh, M., 2003. A graph-theoretical approach for comparison of observational galaxy distributions with cosmological n-body simulations. *A&A* 399, 1–7. URL: <https://doi.org/10.1051/0004-6361:20021607>, doi:10.1051/0004-6361:20021607.

Veenstra, P., Cooper, C., Phelps, S., 2017. Spectral clustering using the knn-mst similarity graph. *IEEE*, 222–227 URL: <https://ieeexplore.ieee.org/abstract/document/7835917>, doi:10.1109/CEEC.2016.7835917.

Vega, O., Clemens, M. S., Bressan, A., Granato, G. L., Silva, L., Panuzzo, P., 2008. Modelling the spectral energy distribution of ulirgs* - ii. the energetic environment and the dense interstellar medium. *A&A* 484, 631–653. URL: <https://doi.org/10.1051/0004-6361:20078883>, doi:10.1051/0004-6361:20078883.

Veilleux, S., Rupke, D.S.N., Kim, D.C., Genzel, R., Sturm, E., Lutz, D., Contursi, A., Schweitzer, M., Tacconi, L.J., Netzer, H., et al., 2009. Spitzer quasar and ulirg evolution study (quest). iv. comparison of 1 jy ultraluminous infrared galaxies with palomar-green quasars. *ApJS* 182, 628. URL: <http://dx.doi.org/10.1088/0067-0049/182/2/628>, doi:10.1088/0067-0049/182/2/628.

Werner, M.W., Roellig, T.L., Low, F.J., Rieke, G.H.a., 2004. The spitzer space telescope mission. *ApJS* 154, 1–9. URL: <https://doi.org/10.1086/422992>, doi:10.1086/422992.

Yuan, T.T., Kewley, L.J., Sanders, D.B., 2010. THE ROLE OF STARBURST-ACTIVE GALACTIC NUCLEUS COMPOSITES IN LUMINOUS INFRARED GALAXY MERGERS: INSIGHTS FROM THE NEW OPTICAL CLASSIFICATION SCHEME. *ApJ* 709, 884–911. URL: <https://doi.org/10.1088/0004-637x/709/2/884>, doi:10.1088/0004-637x/709/2/884.

Appendix A.

The spectral clustering algorithm proposed by Shi and Malik (2000) consists of the following steps:

- (1) First, we compute the *affinity matrix* using the Gaussian Kernel. Then, we apply the k -nearest neighbour method (see Section (4.1), to extract the sparse, weighted SED similarity graph $G(V, E, \mathbf{W})$.
- (2) We compute the *unnormalized Laplacian* of the graph $G(V, E, \mathbf{W})$, $\mathbf{L}: \mathbf{L} = \mathbf{L} - \mathbf{W}$.
- (3) We compute the k *eigenvectors* x_1, \dots, x_k of $\mathbf{L}: \mathbf{L}\mathbf{X} = \lambda\mathbf{D}\mathbf{X}$, where k^6 is given as input, \mathbf{D} = the diagonal matrix, with D_{ii} = the sum of the i -th row of \mathbf{W} , $\mathbf{X} = [x_1, x_2, \dots, x_k]$ is a $N \times k$ matrix containing the k -largest generalized eigenvectors of \mathbf{L} and λ is scalar, the *eigenvalue* of \mathbf{L} .
- (4) We apply the k -means clustering algorithm on the $N \times k$ matrix $\mathbf{X} = [x_1 x_2 \dots x_k]$ and assign each node $i \in [N]$ to the cluster in which row i of matrix \mathbf{X} is assigned.

Appendix B.

The graphs resulting from the application of several community detection clustering algorithms are displayed in this section. The clustering algorithms implemented are:

1. Louvain algorithm of Blondel et al. (2008b).
2. Edge betweenness algorithm of Girvan and Newman (2002).
3. Leiden algorithm of Traag et al. (2019).
4. Leading eigenvector algorithm of Newman (2004).
5. Walktrap algorithm of Pons and Latapy (2006).
6. Spectral clustering algorithm of Ng et al. (2001).
7. Spectral clustering algorithm of Shi and Malik (2000).

⁶Note that this parameter k is unrelated to the parameter k used for the k -nearest neighbour method applied before. We use the same letter, since this is the typically used letter in both methods (k -nearest-neighbours and spectral graph clustering).

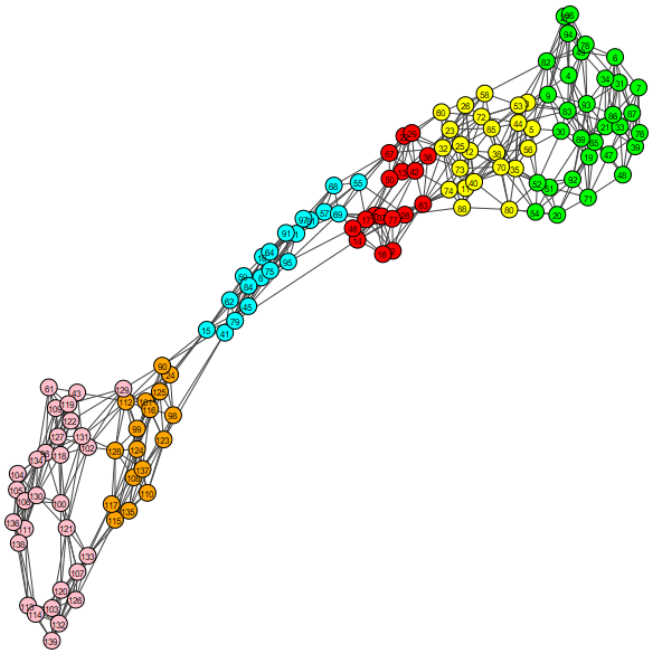


Figure B.1: Communities detected using the Louvain clustering algorithm of Blondel et al. (2008b). Six communities were detected with an optimal modularity of 0.6974 and a max conductance of 0.2209.

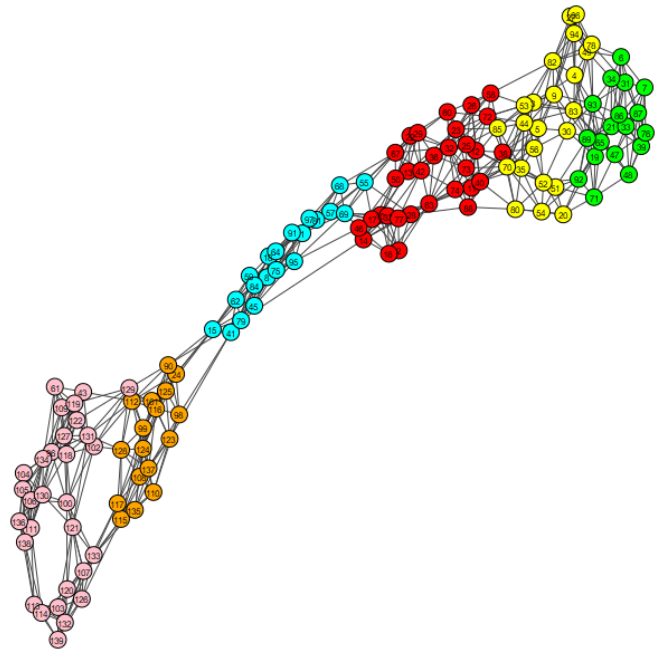


Figure B.3: Communities detected using the Leiden clustering algorithm of Traag et al. (2019). Six communities were detected with a resolution parameter = 1.0, resulting in an optimal modularity of 0.6959 and a conductance of 0.3069.

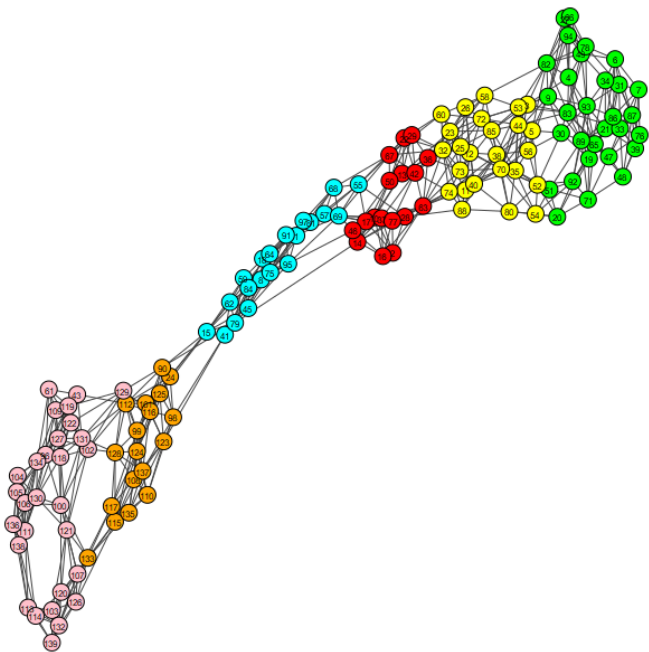


Figure B.2: Communities detected using the edge-betweenness clustering algorithm of Girvan and Newman (2002). Six communities were detected with an optimal modularity of 0.6965 and max conductance of 0.2209.

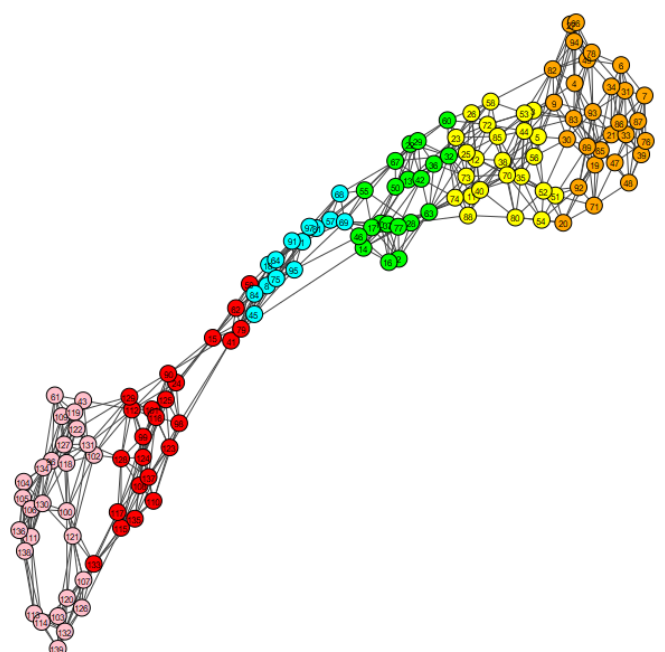


Figure B.4: Communities detected using the leading eigenvector clustering algorithm of Newman (2004). Six communities were detected with an optimal modularity of 0.6711 and max conductance of 0.2288.

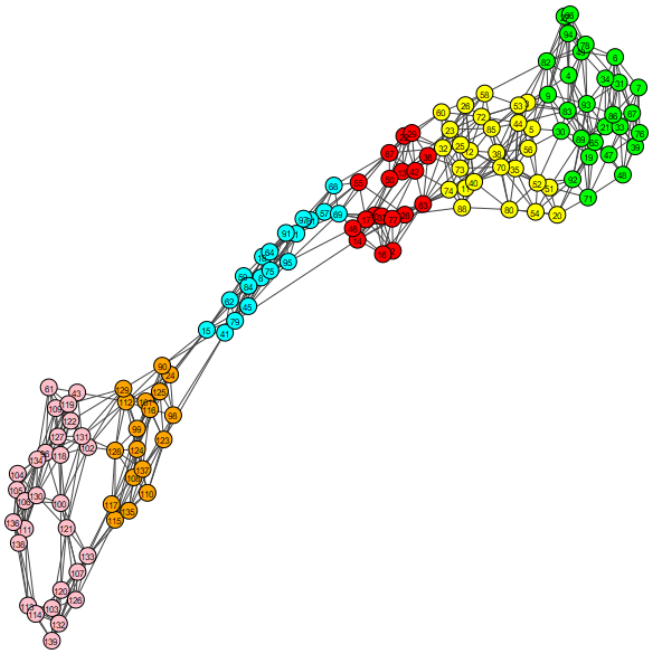


Figure B.5: Communities detected based on the random walks community detection algorithm of Pons and Latapy (2006). Six communities were detected with an optimal modularity of 0.7012 and max conductance of 0.2103.

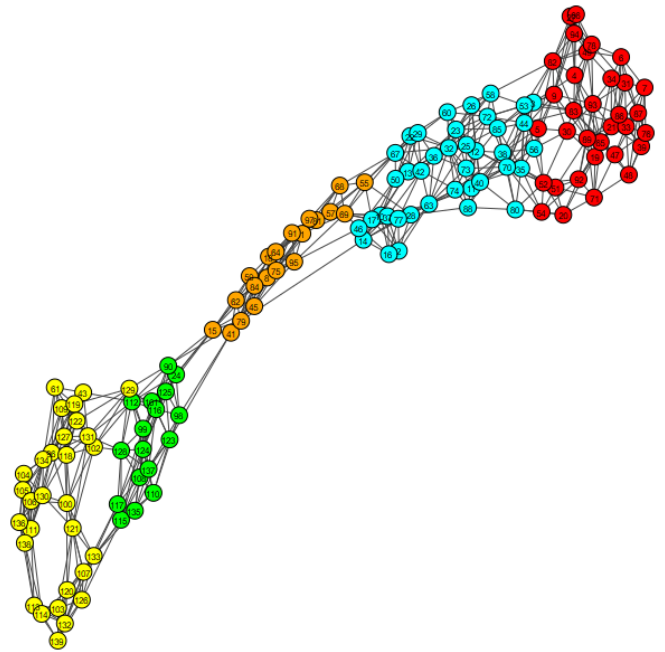


Figure B.7: Communities detected using the spectral clustering algorithm of Shi and Malik (2000), with a preset of 5 clusters. The maximum conductance was calculated as 0.0588 and the modularity score as 0.6899.

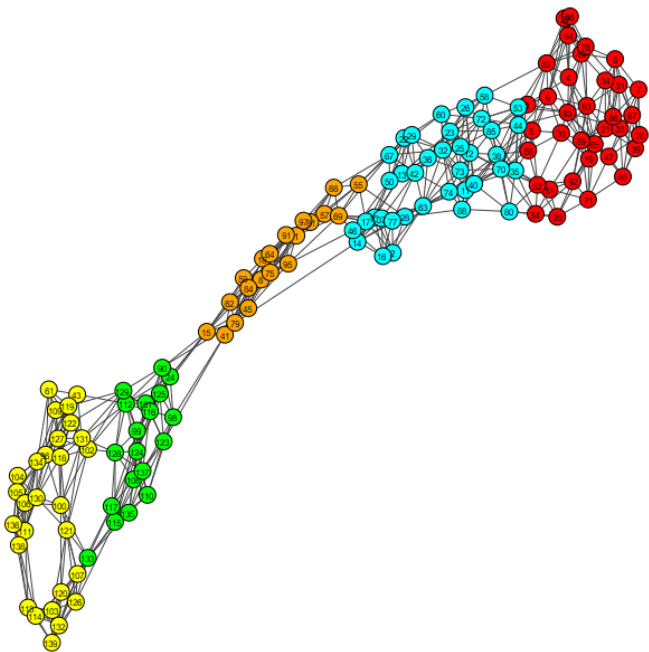


Figure B.6: Communities detected using the spectral clustering algorithm of Ng et al. (2001), with a preset of 5 clusters. The maximum conductance was calculated as 0.0526 and the modularity score as 0.6841.

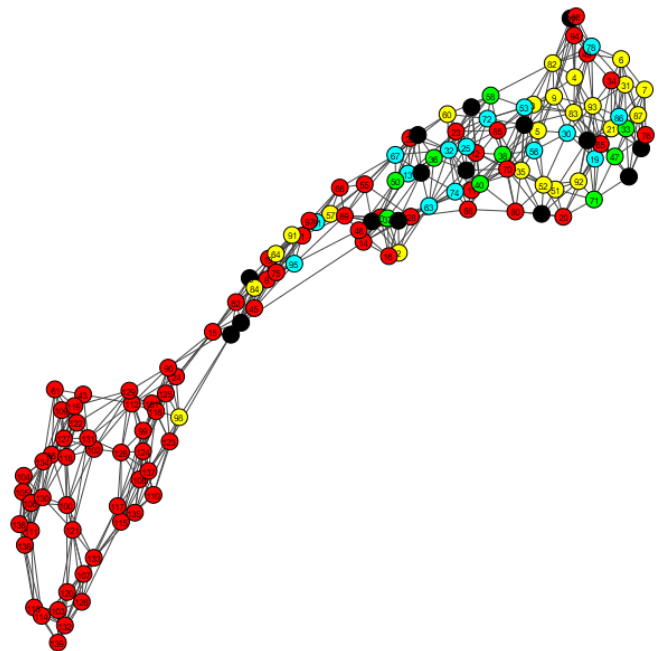


Figure B.8: Our graph colored based on the nuclear separation of ULIRGs, where data is available. Nuclear separation distance ranges are set (in kiloparsecs) similar to Farrah et al. (2009) as: Black: unavailable data, Cyan: > 12 kpc, Green: 6 - 12 kpc, Yellow: 0.1 - 6 kpc, Red: < 0.1 kpc (single nucleus).

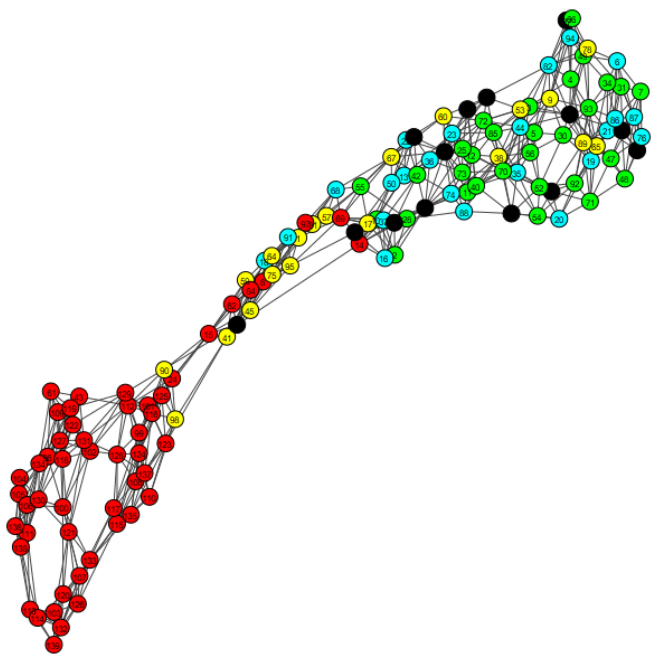


Figure B.9: Our graph colored based on the optical spectral type of ULIRGs, where data is available. Optical spectral type per color is taken similar to Farrah et al. (2009) as:
Black = unavailable data, Cyan = H_{II} , Green = LINER, Yellow = Seyfert-2, Red = Seyfert-1/quasars.

Appendix C.

Table A.1: Reference table of galaxy names and labels used in graphs.

1	IRAS 05189-2524	36	IRAS 06009-7716	71	IRAS 16300+1558	106	PG 1151+117
2	IRAS 08572+3915	37	IRAS 06035-7102	72	IRAS 16334+4630	107	PG 1307+085
3	IRAS 12112+0305	38	IRAS 06206-6315	73	IRAS 16576+3553	108	PG 1309+355
4	IRAS 14348-1447	39	IRAS 06301-7934	74	IRAS 17068+4027	109	PG 1402+261
5	IRAS 15250+3609	40	IRAS 06361-6217	75	IRAS 17179+5444	110	PG 1501+106
6	IRAS 22491-1808	41	IRAS 07145-2914	76	IRAS 17208-0014	111	PG 1535+547
7	Arp 220	42	IRAS 07449+3350	77	IRAS 17252+3659	112	I Zw 1
8	Mrk 231	43	IRAS 07598+6508	78	IRAS 17463+5806	113	PG 0049+171
9	Mrk 273	44	IRAS 08208+3211	79	IRAS 18030+0705	114	PG 0921+525
10	UGC 5101	45	IRAS 08559+1053	80	IRAS 18443+7433	115	PG 0923+129
11	IRAS F00183-7111	46	IRAS 09022-3615	81	IRAS 19254-7245	116	PG 0934+013
12	IRAS 00188-0856	47	IRAS 09463+8141	82	IRAS 19297-0406	117	PG 1011-040
13	IRAS 00199-7426	48	IRAS 10091+4704	83	IRAS 19458+0944	118	PG 1012+008
14	IRAS 00275-0044	49	IRAS 10378+1109	84	IRAS 20037-1547	119	PG 1022+519
15	IRAS 00275-2859	50	IRAS 10565+2448	85	IRAS 20087-0308	120	PG 1048+342
16	IRAS 00397-1312	51	IRAS 11038+3217	86	IRAS 20100-4156	121	PG 1114+445
17	IRAS 00406-3127	52	IRAS 11095-0238	87	IRAS 20414-1651	122	PG 1115+407
18	IRAS 01003-2238	53	IRAS 11223-1244	88	IRAS 20551-4250	123	PG 1149-110
19	IRAS 01199-2307	54	IRAS 11582+3020	89	IRAS 21272+2514	124	PG 1202+281
20	IRAS 01298-0744	55	IRAS 12018+1941	90	IRAS 23060+0505	125	PG 1244+026
21	IRAS 01355-1814	56	IRAS 12032+1707	91	IRAS 23128-5919	126	PG 1310-108
22	IRAS 01388-4618	57	IRAS 12072-0444	92	IRAS 23129+2548	127	PG 1322+659
23	IRAS 01494-1845	58	IRAS 12205+3356	93	IRAS 23230-6926	128	PG 1341+258
24	IRAS 02054+0835	59	IRAS 12514+1027	94	IRAS 23253-5415	129	PG 1351+236
25	IRAS 02113-2937	60	IRAS 13120-5453	95	IRAS 23498+2423	130	PG 1404+226
26	IRAS 02115+0226	61	IRAS 13218+0552	96	3C 273	131	PG 1415+451
27	IRAS 02455-2220	62	IRAS 13342+3932	97	Mrk 1014	132	PG 1416-129
28	IRAS 02530+0211	63	IRAS 13352+6402	98	Mrk 463E	133	PG 1448+273
29	IRAS 03000-2719	64	IRAS 13451+1232	99	PG 1119+120	134	PG 1519+226
30	IRAS 03158+4227	65	IRAS 14070+0525	100	PG 1211+143	135	PG 1534+580
31	IRAS 03521+0028	66	IRAS 14378-3651	101	PG 1351+640	136	PG 1552+085
32	IRAS 03538-6432	67	IRAS 15001+1433	102	PG 2130+099	137	PG 1612+261
33	IRAS 04114-5117	68	IRAS 15206+3342	103	PG 0052+251	138	PG 2209+184
34	IRAS 04313-1649	69	IRAS 15462-0450	104	PG 0804+761	139	PG 2304+042
35	IRAS 04384-4848	70	IRAS 16090-0139	105	PG 1116+215		

Appendix D.

Table A.2: Table of galaxy names and the calculated values for PAH emission equivalent widths at $6.2\mu\text{m}$ and $11.2\mu\text{m}$ and the silicate absorption strength at $9.7\mu\text{m}$ of our sample.

Name	PAH $6.2\mu\text{m}$ ew	PAH $11.2\mu\text{m}$ ew	Si $9.7\mu\text{m}$	Name	PAH $6.2\mu\text{m}$ ew	PAH $11.2\mu\text{m}$ ew	Si $9.7\mu\text{m}$
3C 273	0.01	0.01	0.01	IRAS 17068+4027	0.21	0.30	-1.82
Arp 220	0.37	0.35	-3.08	IRAS 17179+5444	0.16	0.07	-0.32
IRAS 01388-4618	0.70	0.50	-1.41	IRAS 17208-0014	0.63	0.62	-2.31
IRAS 02113-2937	0.76	0.48	-1.74	IRAS 17252+3659	0.41	0.32	-2.12
IRAS 02530+0211	0.04	0.04	-3.34	IRAS 17463+5806	0.37	0.65	-2.07
IRAS 03000-2719	0.52	0.30	-0.79	IRAS 18030+0705	0.91	0.72	-1.02
IRAS 04384-4848	0.52	0.40	-2.28	IRAS 18443+7433	0.14	0.21	-3.05
IRAS 06009-7716	0.85	0.55	-1.77	IRAS 19254-7245south	0.09	0.15	-1.42
IRAS 07145-2914	0.06	0.08	-0.67	IRAS 19297-0406	0.64	0.51	-1.75
IRAS 08559+1053	0.32	0.30	-0.76	IRAS 19458+0944	0.75	0.50	-1.95
IRAS F00183-7111	0.04	0.07	-2.62	IRAS 20037-1547	0.08	0.06	-0.24
IRAS 00188-0856	0.09	0.32	-2.34	IRAS 20087-0308	0.55	0.60	-1.91
IRAS 00199-7426	0.65	0.50	-1.56	IRAS 20100-4156	0.20	0.48	-2.40
IRAS 00275-0044	0.37	0.40	-1.42	IRAS 20414-1651	0.86	0.54	-2.08
IRAS 00275-2859	0.03	0.05	-0.40	IRAS 20551-4250	0.15	0.26	-2.81
IRAS 00397-1312	0.03	0.14	-2.70	IRAS 21272+2514	0.30	0.49	-2.10
IRAS 00406-3127	0.07	0.09	-1.90	IRAS 22491-1808	0.66	0.55	-1.84
IRAS 01003-2238	0.06	0.01	-0.83	IRAS 23128-5919	0.45	0.20	-1.23
IRAS 01199-2307	0.21	0.34	-2.82	IRAS 23129+2548	0.10	0.50	-2.96
IRAS 01298-0744	0.01	0.29	-3.42	IRAS 23230-6926	0.50	0.48	-2.28
IRAS 01355-1814	0.32	0.25	-2.64	IRAS 23253-5415	0.31	0.36	-1.17
IRAS 01494-1845	0.82	0.54	-1.77	IRAS 23498+2423	0.09	0.06	-0.75
IRAS 02054+0835	0.01	0.01	-0.18	Mrk 1014	0.08	0.07	-0.11
IRAS 02115+0226	0.36	1.03	-0.83	Mrk 231	0.03	0.02	-0.81
IRAS 02455-2220	0.68	0.41	-2.12	Mrk 273	0.30	0.29	-1.99
IRAS 03158+4227	0.14	0.22	-2.72	Mrk 463E	0.01	0.01	-0.45
IRAS 03521+0028	0.70	0.49	-1.54	PG 1119+120	0.01	0.03	0.03
IRAS 03538-6432	0.26	0.29	-1.57	PG 1211+143	0.01	0.00	0.11
IRAS 04114-5117	0.71	0.61	-1.63	PG 1351+640	0.03	0.04	0.56
IRAS 04313-1649	0.22	0.37	-3.08	PG 2130+099	0.01	0.00	-0.09
IRAS 05189-2524	0.04	0.06	-0.54	UGC 5101	0.35	0.35	-1.86
IRAS 06035-7102	0.14	0.23	-1.49	WIR-IRAS 23060+0505	0.02	0.01	-0.40
IRAS 06206-6315	0.25	0.28	-1.94	I Zw 1	0.00	0.02	0.20
IRAS 06301-7934	0.39	0.63	-2.12	PG 0049+171	0.01	0.00	0.13
IRAS 06361-6217	0.11	0.20	-2.62	PG0052+251	0.00	0.04	0.11
IRAS 07449+3350	0.35	0.31	-1.12	PG0804+761	0.01	0.00	0.34
IRAS 07598+6508	0.02	0.01	0.10	PG 0921+525	0.00	0.01	0.14
IRAS 08208+3211	0.70	0.59	-1.18	PG 0923+129	0.04	0.06	-0.07
IRAS 08572+3915	0.04	0.08	-3.82	PG 0934+013	0.04	0.05	-0.04
IRAS 09022-3615	0.20	0.25	-1.40	PG 1011-040	0.01	0.03	0.26
IRAS 09463+8141	0.51	0.47	-1.36	PG 1012+008	0.01	0.01	0.11
IRAS 10091+4704	0.07	0.33	-2.37	PG 1022+519	0.09	0.16	-0.08
IRAS 10378+1109	0.10	0.30	-1.82	PG 1048+342	0.03	0.02	-0.05
IRAS 10565+2448	0.70	0.44	-1.55	PG 1114+445	0.00	0.01	0.02
IRAS 11038+3217	0.17	0.42	-3.58	PG 1115+407	0.06	0.09	-0.09
IRAS 11095-0238	0.04	0.24	-2.72	PG 1116+215	0.00	0.01	0.08
IRAS 11223-1244	0.33	0.48	-1.85	PG 1149-110	0.01	0.02	-0.05
IRAS 11582+3020	0.11	0.36	-2.66	PG 1151+117	0.26	0.05	0.12
IRAS 12018+1941	0.17	0.07	-1.70	PG 1202+281	0.02	0.03	0.11
IRAS 12032+1707	0.01	0.40	-2.57	PG 1244+026	0.03	0.03	0.05
IRAS 12072-0444	0.15	0.07	-1.52	PG 1307+085	0.11	0.04	0.02
IRAS 12112+0305	0.61	0.51	-1.70	PG 1309+355	0.01	0.03	0.22
IRAS 12205+3356	0.65	0.41	-1.34	PG 1310-108	0.00	0.02	0.10
IRAS 12514+1027	0.00	0.03	-1.53	PG 1322+659	0.03	0.03	0.04
IRAS 13120-5453	0.71	0.47	-1.85	PG 1341+258	0.02	0.01	0.06
IRAS 13218+0552	0.00	0.00	-0.55	PG 1351+236	0.26	0.30	-0.33
IRAS 13342+3932	0.16	0.08	-0.07	PG 1402+261	0.01	0.04	0.09
IRAS 13352+6402	0.12	0.21	-2.09	PG 1404+226	0.03	0.04	0.16
IRAS 13451+1232	0.01	0.00	-0.50	PG 1415+451	0.01	0.07	-0.04
IRAS 14070+0525	0.12	0.40	-2.68	PG 1416-129	0.03	0.05	0.01
IRAS 14348-1447	0.49	0.56	-1.73	PG 1448+273	0.02	0.04	-0.00
IRAS 14378-3651	0.74	0.39	-1.93	PG 1501+106	0.01	0.01	-0.14
IRAS 15001+1433	0.29	0.23	-1.16	PG 1519+226	0.00	0.03	-0.00
IRAS 15206+3342	0.46	0.27	-0.86	PG 1534+580	0.01	0.03	0.00
IRAS 15250+3609	0.03	0.31	-3.14	PG 1535+547	0.00	0.02	-0.01
IRAS 15462-0450	0.09	0.07	-0.53	PG 1552+085	0.02	0.02	0.15
IRAS 16090-0139	0.13	0.40	-2.24	PG 1612+261	0.00	0.03	-0.01
IRAS 16300+1558	0.14	0.36	-2.55	PG 2209+184	0.04	0.05	0.08
IRAS 16334+4630	0.60	0.53	-1.64	PG 2304+042	0.01	0.01	0.17
IRAS 16576+3553	0.48	0.61	-1.21				